RESEARCH ARTICLE

Key Points:

- We build synthetic frequency-longitude maps of polarized Jovian auroral radio emissions, DAM, HOM, and bKOM
- Jovian HOM and DAM are dominantly rotation-modulated, bKOM dominantly solar wind-modulated
- HOM appears primarily connected to decameter sources from the dusk side of the Jovian magnetosphere

Correspondence to:

P. Zarka,
philippe.zarka@obspm.fr

Jupiter's Auroral Radio Emissions Observed by Cassini: Rotational Versus Solar Wind Control, and Components Identification

P. Zarka[1,2] , F. P. Magalhães[1] , M. S. Marques[3] , C. K. Louis[4,5] , E. Echer[6] , L. Lamy[1,2] , B. Cecconi[1,2] , and R. Prangé[1]

[1]LESIA, Observatoire de Paris, CNRS, PSL, Sorbonne Université, Université de Paris, Meudon, France, [2]Station de Radioastronomie de Nançay, USN, Observatoire de Paris, CNRS, PSL, Université d'Orléans, Nançay, France, [3]Departamento de Geofsica, Universidade Federal do Rio Grande do Norte, Natal, Brazil, [4]School of Cosmic Physics, DIAS Dunsink Observatory, Dublin Institute for Advanced Studies, Dublin, Ireland, [5]Institut de Recherche en Astrophysique et Planétologie (IRAP), Université de Toulouse, CNRS, CNES, UPS, Toulouse, France, [6]Instituto Nacional de Pesquisas Espaciais—INPE, São José dos Campos, Brazil

Abstract Reanalyzing Cassini radio observations performed during Jupiter's flyby of 2000–2001, we study the internal (rotational) versus external (solar wind) control of Jupiter's radio emissions, from kilometer to decameter wavelengths, and the relations between the different auroral radio components. For that purpose, we build a database of the occurrence of Jovian auroral radio components bKOM, HOM, and DAM observed by Cassini, and then frequency-longitude stacked plots of the polarized intensity of these radio components. Comparing the results obtained inbound and outbound, as a function of the Observer's or Sun's longitude, we find that HOM & DAM are dominantly rotation-modulated (i.e., emitted from searchlight-like sources fixed in Jovian longitude), whereas bKOM is modulated more strongly by the solar wind than by the rotation (i.e., emitted from sources more active within a given Local Time sector). We propose a simple analytical description of these internal and external modulations and evaluate its main parameters (the amplitude of each control) for HOM + DAM and bKOM. Comparing Cassini and Nançay Decameter Array data, we find that HOM is primarily connected to the decameter emissions originating from the dusk sector of the Jovian magnetosphere. HOM and DAM components form a complex but stable pattern in the frequency-longitude plane. HOM also seems to be related to the "lesser arcs" identified by Voyager. bKOM consists of a main part above ~40 kHz in antiphase with HOM occurrence, and detached patches below ~80 kHz in phase with HOM. The frequency-longitude patterns formed by DAM, HOM and bKOM remain to be modeled.

1. Introduction

Since their discovery by Burke and Franklin (1955) Jupiter's magnetospheric radio emissions have been the subject of many studies, based on ground- and space-based observations. These studies are motivated by at least four objectives: (a) fully understand the phenomenology and source locations of the Jovian radio components (Zarka, 1998, & references therein), as well as (b) their generation processes (Treumann, 2006, & references therein), (c) use them—as well as optical observations of aurora—as diagnostics of the magnetospheric dynamics (rotation, convection, response to interplanetary shocks—[see Hess et al., 2014, & references therein]), and more recently (d) extrapolate them to possible exoplanetary counterparts (Zarka et al., 2018).

The phenomenology of Jovian radio emissions is by far the most complex of all known planetary radio emissions (see e.g., Figure 1 of Zarka et al., 2001). With the development of a radio simulation code (named ExPRES) based on the cyclotron Maser instability (CMI) mechanism (S. Hess et al., 2008; Louis, Hess, et al., 2019; Louis, Lamy, Zarka, Cecconi, Hess, & Bonnin, 2017; Louis, Lamy, Zarka, Cecconi, Imai, et al., 2017) and high-latitude or, even, in-source measurements by the Juno mission (Kurth, Imai, et al., 2017; Louarn et al., 2017, 2018), significant progress has been made on objective (b), confirming the role of the loss cone driven CMI in the generation of high-latitude radio components on the extraordinary—X—magnetoionic mode (whereas the narrowband kilometer component—nKOM—is produced at the local plasma frequency in the Io plasma torus (Reiner et al., 1993), probably on the ordinary mode).

Objective (a) has also progressed notably since the review of Zarka (1998). Many results (identification, characteristics) have been obtained concerning satellite-driven decameter (DAM) emissions (Louis, Lamy, Zarka, Cecconi, & Hess, 2017; Marques et al., 2017; Zarka et al., 2018), that are out of the scope of this paper. The source locations of hectometer (HOM) and broadband kilometer (bKOM) emissions have received considerable attention. They were initially found by Ladreiter et al. (1994) to lie along magnetic field lines with L-shells 7 to 9 for HOM (apex 7 to 11 Jovian radii—R_J—, within the inner magnetosphere) and L-shells 9 to 15 for bKOM (apex between 9 and >50 R_J, possibly closing in the distant outer magnetosphere or opened to the solar wind). These source locations were confirmed for HOM and bKOM from Ulysses measurements (Zarka et al., 2001), and for bKOM from Juno measurements with an emphasis on larger apex distances, ~40–60 R_J (Imai et al., 2019). The statistical study of in-situ source crossings by Juno from Louis, Prangé, et al. (2019) extended outwards the range of HOM source field line apex (~12–58 R_J), whereas bKOM source field apex were found mostly in the range 14–66 R_J, thus largely overlapping with HOM. The source of the auroral DAM (also called non-Io-DAM, but auroral DAM is now to be preferred following the discovery of Ganymede-induced and Europa-induced DAM [Louis, Lamy, Zarka, Cecconi, & Hess, 2017; Zarka et al., 2017, 2018]) was long thought to be "colocated with the main UV auroral oval" (Bagenal et al., 2017). Louis, Prangé, et al. (2019) were able to directly measure it from 26 Juno source crossings, and found a range of apex 7–61 R_J. Thus bKOM, HOM, and auroral DAM sources locations all overlap and correlate (at least partly) with the main UV auroral oval, with the lower limit of their source field lines apex ordered as DAM ≤ HOM ≤ bKOM.

In relation with objective (c) these localization results are consistent with the solar wind control exerted to various extents on bKOM, HOM, and auroral DAM (Echer et al., 2010; S. L. G. Hess et al., 2012; Hess et al., 2014; Zarka, 1998, & references therein), that are also controlled by Jupiter's rotation (the so-called "pulsar-like" behavior of Jovian radio emissions [Dessler, 1983]). But they do not enlighten our understanding of the relative role of external (solar wind) versus internal (rotation) control on each radio component, nor the relationship between radio components: for example, HOM was often proposed to be the low frequency extent of auroral DAM, but without any direct proof of it (Bagenal et al., 2017; Zarka, 1998, & references therein). These are the two questions addressed in the present paper.

For that purpose, we re-analyze Cassini radio flux density data, taking into account the polarization information. Cassini radio flux density observations around the Jupiter flyby have been previously analyzed by Zarka et al. (2004), who derived the spectral range and flux density spectrum of each Jovian radio component, as well as related quantities (variability, beam solid angle, and average power), and by Imai et al. (2011) who analyzed frequency-longitude distributions of HOM and DAM occurrence. Here we analyze frequency-longitude distributions of circularly polarized flux density over the whole spectral range of the Cassini-RPWS-HFR instrument (Gurnett et al., 2004), in order to better characterize the frequency-longitude-polarization structure of all Jovian auroral radio components (auroral DAM—that we will hereafter simply call "DAM"—, HOM and bKOM), the relationships between these components, and compare their rotational control to their control by the solar wind. For this study, we also use a new way of analyzing space-borne radio observations of Jupiter (potentially applicable to other planetary radio emissions), inspired from the Nançay Decameter Array's Jupiter database of Marques et al. (2017), that involves the construction of a catalog of the detected emissions per radio component prior to their statistical analysis.

Section 2 describes the Cassini data and its re-processing. Section 3 presents the construction of the catalog and a first statistical analysis of the data based on it. Section 4 compares our analysis of the polarized flux density with longitude-frequency occurrence distributions of Imai et al. (2011). Section 5 focuses on the rotational versus solar wind control of bKOM, HOM and DAM components. Section 6 discusses the relationship between polarized radio components from Section 4, further relying on the identification of their high-frequency extent in the Nançay–Jupiter database. Finally, Section 7 summarizes our findings and provides perspectives for the subsequent analysis of Juno radio data.
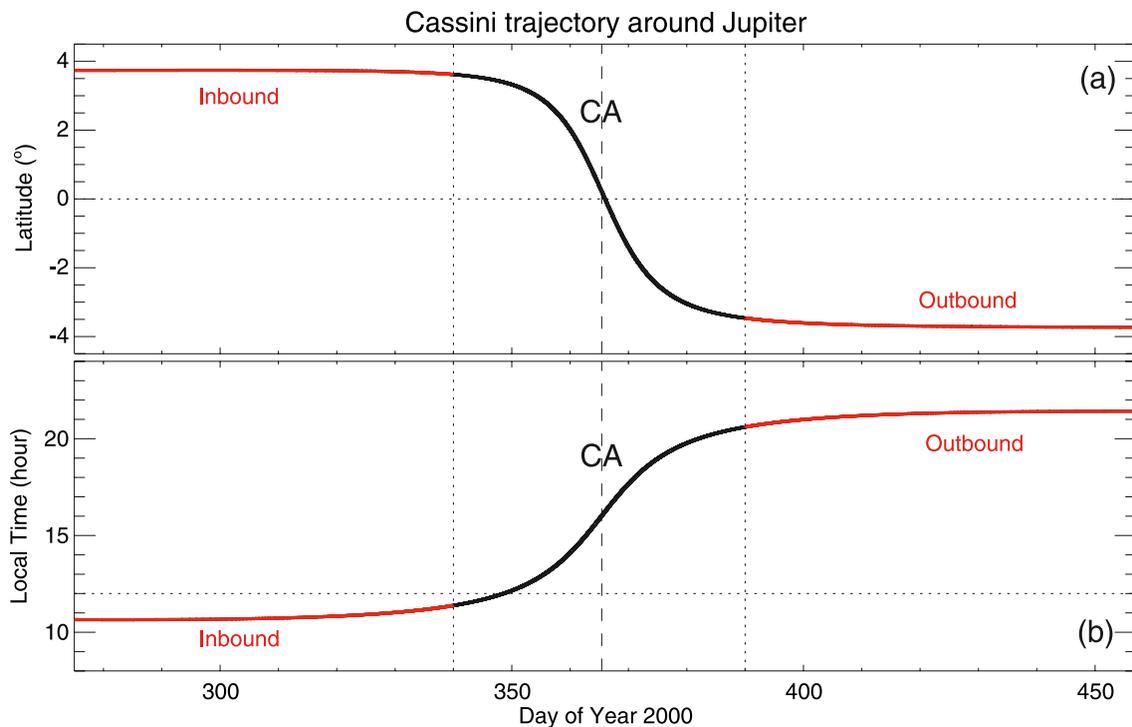
Figure 1. Cassini's latitude (a) and local time (b) over the 6-month interval studied around Jupiter. Time is counted as day of year (DoY) 2000. We distinguish 3 intervals: the inbound leg from DoY 275.0 to DoY 340.0, with latitude ~+3.7° and local time (LT) ~10.7 hr; the outbound leg from day 390.0 to day 457.0, with latitude ~−3.7° and LT ~21.4 h; the near-closest approach (CA) interval in between. CA occurred on DoY 365.41667.

2. Data and Processing

The Cassini-RPWS-HFR (Radio and Plasma Wave Science—High Frequency Receiver, hereafter simply RPWS [Gurnett et al., 2004]) data analyzed in this paper are the same as in Zarka et al. (2004), except that we considered not only the flux density S (in Wm^{-2}Hz^{-1}) but also the circular polarization fraction V (−1 ≤ V ≤ 1) with V = −1 corresponding to right-hand (RH) circular polarization and V = +1 to the left-hand (LH) sense.

Cassini's closest approach (CA) to Jupiter occurred on Dec. 30th, 2000, 10 hr (Day 365.41667 of year 2000), at a minimum distance ~137R_J. Our data cover an interval of 6 months around CA, from October 1st, 2000, 0 hr (Day 275.0 of year 2000) to March 31st, 2001, 24 hr (Day 457.0 of year 2000—counting the time from January 1st, 2000 provides a convenient monotonic time scale). Information about the Cassini trajectory during the Jupiter flyby is displayed in Figure 1. Cassini's latitude varies from + 3.74° (inbound) to − 3.73° (outbound), whereas its local time (LT) varies from 10.65 hr (inbound) to 21.42 hr (outbound). In our study, we will distinguish the inbound and outbound legs over which the latitude and LT remain nearly constant, from the near-CA interval where these parameters change quickly.

Flux density data consist as in Zarka et al. (2004) of average RPWS measurements interpolated on a regular grid of 206 frequencies (48 log-spaced channels from 3.5 to 320 kHz, and 158 lin-spaced channels of 100 kHz width from 375 to 16,075 kHz) and a linear time ramp of 90 s steps (960 spectra/day × 182 days = 174,720 time steps). Measurements were calibrated in flux density using the Galactic background, and then the average Galactic background was subtracted, the excess being normalized to a distance of 1 AU from Jupiter. The resulting values, displayed in Figure A1, still reveal a variation with Cassini's distance to Jupiter. In order to improve the quality of our subsequent analysis, we detrended these data as explained in Appendix A.

The Cassini-RPWS-HFR receiver provides auto- and cross-correlation of the RPWS electric antenna signals, the inversion of which allowed us to retrieve the polarization of the incoming waves (4 Stokes parameter S = flux density, U & Q characterizing the linear polarization, and V = circular polarization) (Cecconi & Zarka, 2005). For emissions on the X-mode, the sign of V indicates the hemisphere of origin: RH emissions
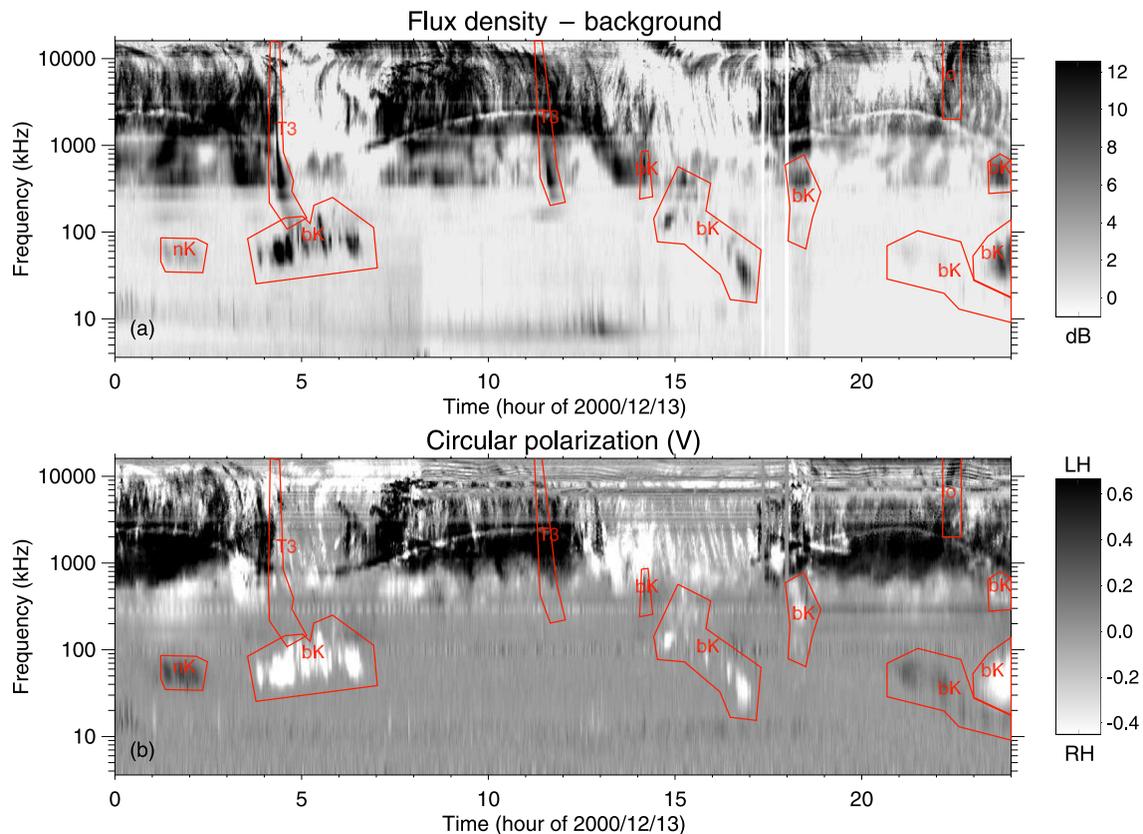
Figure 2. Example of 24-hr dynamic spectra (from 2000/12/13, i.e., day 348 of year 2000) used for building our radio components catalog, with indication of cataloged events (red contours). (a) Detrended flux density measured by RPWS, with background subtracted. The flux density scale is in dB above the background. (b) Circular polarization V. Radio components were visually identified according to their time-frequency morphology and polarization. Cataloged components include solar type III bursts (**T3**, unpolarized thus invisible in panel [b]), Jovian bKOM (**bK**), nKOM (**nK**), and Io-induced DAM (**Io**). Jovian radio components show a clear 10-h periodicity linked to Jupiter's rotation. A curved, 10-hr modulated attenuation "lane" is visible in the range 0.7–3 MHz.

(V < 0) come from the northern magnetic hemisphere (which is also the northern Jovigraphic one), whereas LH emissions (V > 0) come from the southern hemisphere. We computed dynamic spectra of the circular polarization fraction V on the same time–frequency grid as the flux density measurements. In principle, the inversion should return $-1 \le V \le 1$. But due to numerical errors and statistical noise, the resulting values may sometimes be outside this interval. Also, the inversion of auto- and cross-correlation signals is expected to provide reliable values of Q, U, and V in the short dipole approximation, that is, only for frequencies below 2–4 MHz. But we noticed that the sign of V was generally preserved along Jovian DAM emissions up to 16 MHz (see e.g., Figure 2b), providing a good way to discriminate between RH and LH polarized components at all frequencies. As explained in Appendix A, we opted for broad selections of RH ($-1.05 \le V \le -0.02$) and LH ($+0.02 \le V \le +1.05$) polarized signals.

3. Catalog of the Jovian Radio Components

As for all radio experiments on planetary missions, the flux measurements from RPWS are not made by selecting a target field in the sky, but instead integrate all the radio flux received instantaneously from almost the entire sky (Zarka et al., 2004). Angular resolution (~2°) can be restored on isolated intense radiosources by using the cross-correlation signals, through goniopolarimetric inversions (Cecconi & Zarka, 2005), but those are doable only when RPWS is in a specific mode, are valid only in the short dipole approximation ($f \le 2 - 4$ MHz), and they return the direction of the brightest instantaneous source in the sky at any given time–frequency value. Goniopolarimetry was not used during the Jupiter flyby due to the large Cassini-Jupiter distance (always $\ge 137\ R_J$).

Nevertheless, as we will see below, it is very useful to identify and separate the various radio components present in the dynamic spectra. As automated recognition methods are not yet efficient enough, we have created "manually" a catalog of Jupiter's radio components from daily (24 hr) dynamic spectra of detrended flux densities and circular polarizations. Figure 2 displays a typical daily plot. The radio components were visually identified according to their time-frequency morphology and circular polarization, and then manually encircled by contours using a dedicated program that records and draws the same contours in both dynamic spectra whatever the one chosen to encircle an emission.

Cataloged components include: (a) Solar type III bursts (noted **T3**), intense but essentially unpolarized, with a typical negative drift in frequency, very fast above a few MHz and much slower below ~1 MHz; (b) Jovian auroral bKOM (**bK**, sporadic and strongly polarized, typically between ~20 and 400 kHz (Boischot et al., 1981; Carr et al., 1983; Leblanc & Daigne, 1985; Zarka et al., 2004); (c) nKOM from Io's torus (**nK**), smooth and less strongly polarized, restricted to the range ~100–150 kHz (Reiner et al., 1993, 2000); (d) Io- or other satellite-induced DAM emissions (**Io** or **Sa**), identified by comparison with ExPRES simulations (Louis, Hess, et al., 2019; Louis, Lamy, Zarka, Cecconi, & Hess, 2017); (e) a few anomalous events with spurious polarization (**An**); and (vi) unusual extensions of HOM to low frequencies, below ~400 kHz (**Ex**).

In total, ~1800 contours were drawn (332 **T3**, 953 **bK**, 268 **nK**, 141 Io, 41 **Sa**, 55 **An**, and 7 **Ex**) within the 182 pairs of dynamic spectra covering the 6-month interval studied. These contours are then used as inclusive or exclusive masks to select any emission type. For example, all bKOM emission events are selected inclusively using the **bK** label (all emissions outside of **bK** contours are set to zero), whereas auroral DAM emission (that is nearly permanent) is selected by a frequency range (e.g., 3–16 MHz) and excluding **T3**, **Io**, **Sa**, and **An** events. As illustrated in Figure 2, these contours do not need to follow very accurately the emissions because the background contribution is negligible. Their purpose is to separate and label radio components.

In Figure 2, a curved 10-hr modulated attenuation "lane" is visible in the HOM range. It has been interpreted in terms of wave refraction tangent to the Io L-shell (Gurnett et al., 1998; Menietti et al., 2003), and is not discussed further in the present paper.

4. Longitude–Frequency Distributions of Polarized Radio Flux

To study the rotational versus solar wind control of Jovian auroral radio emissions we built, following Imai et al. (2011), stacked intensity plots as a function of longitude and frequency. First, as explained in appendix B, we determined the best way to obtain and display these stacked intensity plots: data selection is made on the basis of our catalog, including bKOM, HOM and DAM components only, with circular polarization measurements in the range $0.02 \leq |V| \leq 1.05$; the stacked dynamic spectra are then divided by their average value at each frequency, equalizing their contrast. The auroral Jovian components show up well in the resulting dynamic spectra, except at low frequencies near CA where they are obscured by very low frequency (VLF) sporadic emissions. We must thus exclude the near-CA interval when stacking emission at low frequencies over the entire flyby. We also demonstrate in Appendix B (Figure B1) the interest of separating the data as a function of their circular polarization sense (sign of V).

In Figure 3 we display inbound (first column) and outbound (second column) stacked dynamic spectra of auroral HOM and DAM, again as a function of longitude and frequency, with polarization information. The frequency scale covers the same range 5–16,125 kHz as in Figure B1, but now with a linear frequency scale, emphasizing HOM and DAM emissions (bKOM is compressed at the bottom of the plots). Longitude bins are 1° wide. The abscissa is Observer's longitude for rows (a) to (d), and Sun's longitude for row (e). HOM clearly shows up as a component distinct from DAM albeit connected to it in the time–frequency plane.

Row (a), reproduced from Figure 4 of Imai et al. (2011), shows occurrence probability above a threshold computed per Jovian rotation. No polarization information is provided (and RFI are visible ≥ 10 MHz). Radio (sub-)components were tentatively identified from their longitude-frequency morphology and labeled in white. We recall that non-Io-A & -B DAM emissions (hereafter simply A & B) originate from the Northern hemisphere, non-Io-C & -D (hereafter simply C & D) from the South, B & D from the West of the observer's meridian (i.e., pre-meridian relative to the planetary rotation), and A & C from the East (i.e., post-meridian) (Hess et al., 2014; Louis, Hess, et al., 2019; Marques et al., 2017).
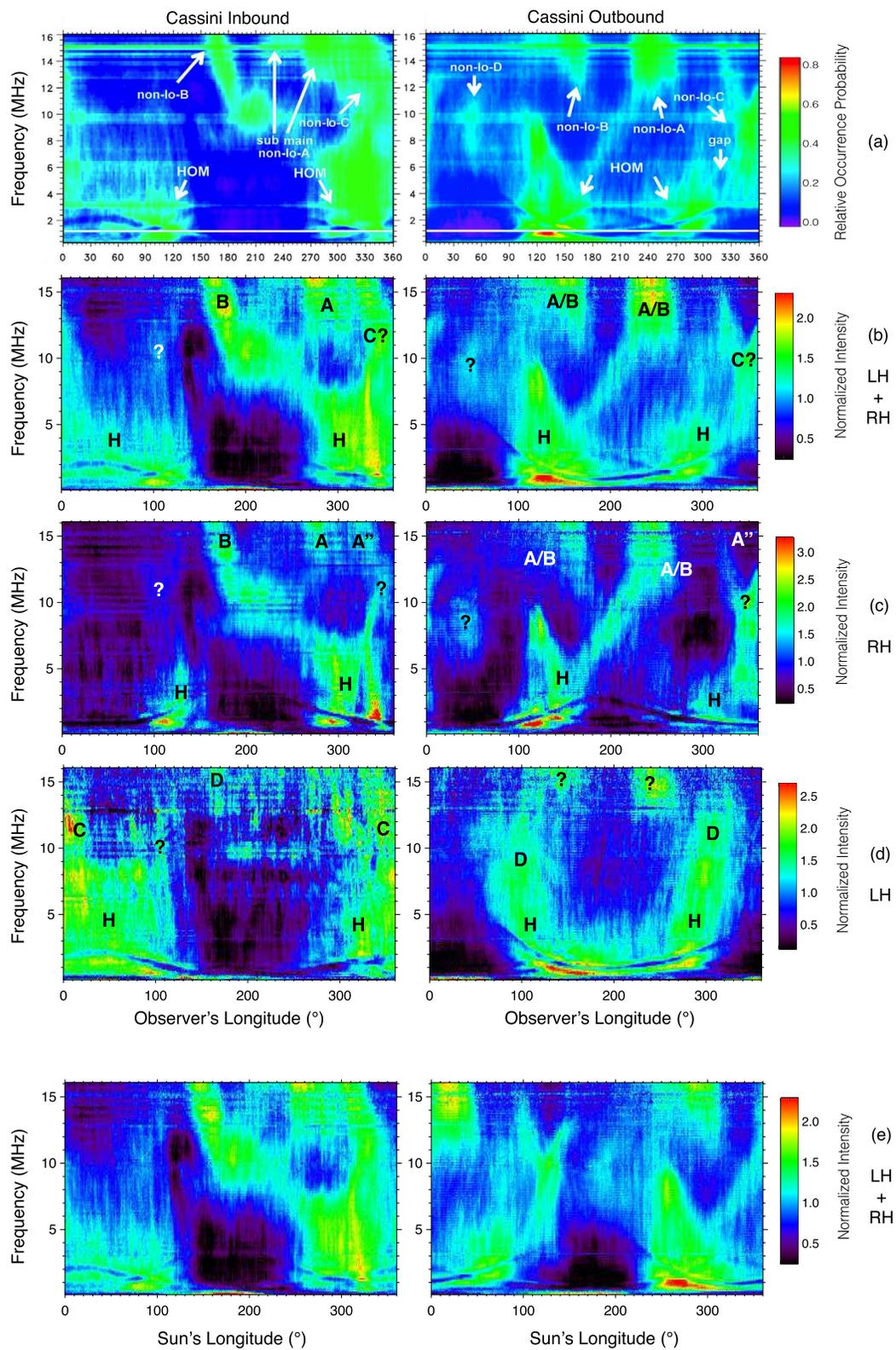
Figure 3.

Row (b) is our version of the same plot from our reprocessed RPWS data, resulting from a selection in polarization ($0.02 \leq |V| \leq 1.05$) and from our catalog (bKOM, HOM, and DAM), as in row (e) of Figure B1, except that here intensities in dB are stacked before normalization by the average value at each frequency, as defined in Figure B1b (stacking linear intensities in Figure B1 provides a sharper comparison of the various selections, while stacking intensities in dB gives more uniform weight to all data and produces more informative plots as in Figure 3). The color scale was adjusted in order to match that of Imai et al. (2011). Our dynamic spectra are fully consistent with Imai's, and at the same time clearer (almost no interference remains, no pollution by any other emission than polarized bKOM, HOM, and DAM, and thus better defined components). Rows (c) and (d) split the dynamic spectra of row (b) in resp. RH and LH polarized auroral emissions. The structure of LH emissions, that are weaker than RH ones, appears clearly on row (d).

The better defined structures seen on rows (b) to (d) raise questions about their identification by Imai et al. (2011). Our identifications of Jovian radio components are labeled in black (or white when superimposed on a dark background), and will be discussed in Section 6. But we can immediately see for example that the bright (yellow) arc labeled **C?** inbound on row (b) (and the emission at longitude $\geq 330°$ also labeled **C?** outbound) are actually RH polarized on row (c), and thus they originate from the northern hemisphere (if on the X mode) and are rather related to a sub-component of non-Io-A DAM, possibly the A″ component identified by Marques et al. (2017).

As in Figures B1e, B1f and B1g, stacked dynamic spectra of Figure 3 look different between inbound and outbound, revealing a control of Jovian auroral radio components that is not purely rotational. This implies that the bKOM, HOM and DAM sources do not behave like searchlight beams. In order to test the role of the solar wind, that causes LT effects in the magnetosphere, we plotted in row (e) the same data as in row (b), but stacked versus the Sun's longitude. As the longitude of Cassini is nearly constant and close to the Sun's along the inbound leg of its fly by trajectory, the left-side dynamic spectra of rows (b) and (e) are very similar. But on the right side, they are shifted by ~ 140°, corresponding to the 9.4 hr shift in LT of Cassini (at 21.4 hr LT outbound) and the Sun (at 12 hr LT). In the Sun's longitude system, the minimum HOM intensity (below ~6 MHz) appears centered at ~180° both inbound and outbound, raising the question of which longitude system better controls auroral emission occurrence. To address this question both for HOM + DAM and for bKOM emissions, we compare quantitatively in the next section stacked dynamic spectra versus each of these two longitude systems.

5. Rotational Versus Solar Wind Control of bKOM, HOM, and DAM

In Figure 4, we study polarized HOM and DAM components in the range 0.8 16.1 MHz, selected from our catalog (excluding **nK**, **T3**, **Io**, **Sa**, **An**, and **bK** events) and with respect to polarization. We compare dynamic spectra now stacked over the entire Cassini-Jupiter flyby (i.e., all three intervals of Figure 1), versus the Observer's longitude in the left-most column, and versus the Sun's longitude in the central column. As we are now stacking ≥430 Jovian rotations in each case, the most relevant longitude system will be the one that organizes the data with the highest contrast. If one picks a wrong reference system, data will be stacked more randomly, resulting in a dynamic spectrum with lower contrast. Integrating each dynamic spectrum over its frequency range, we obtain the plots in the rightmost column of each row.

The qualitative examination of Figure 4 suggests that the contrast of the dynamic spectra is in all cases better when the data is stacked as a function of the Observer's longitude, even in LH polarization. This is confirmed by the larger range covered by the corresponding curves (solid lines) in the rightmost column. After presenting a figure equivalent to Figure 4, but for bKOM, we discuss below the quantitative characterization of the data organization by the two longitude systems.

Figure 3. Inbound (first column) and outbound (second column) stacked dynamic spectra of auroral HOM and DAM versus frequency and Observer's (rows [a–d]) or Sun's longitude (row [e]), in 1° longitude bins. Intensities in dB are stacked and then each row is divided by its average value. The linear frequency scale, emphasizes HOM and DAM while marginalizing bKOM at the bottom of the plots. Row (a) is reproduced from Figure 4 of Imai et al. (2011), with identified radio components labeled in white. Following rows result from our reprocessing of RPWS data, with a selection in polarization ($-1.05 \leq V \leq 0.02$ and/or $0.02 \leq V \leq 1.05$) and from our catalog (bKOM, HOM and DAM). The color scale (in relative units of average flux density at each frequency) has been adjusted to match that of row (a). Our identifications of radio components are labeled in black (or white on a dark background): H stands for HOM; A, B, C, and D for auroral, that is, satellite–independent, decameter emissions.
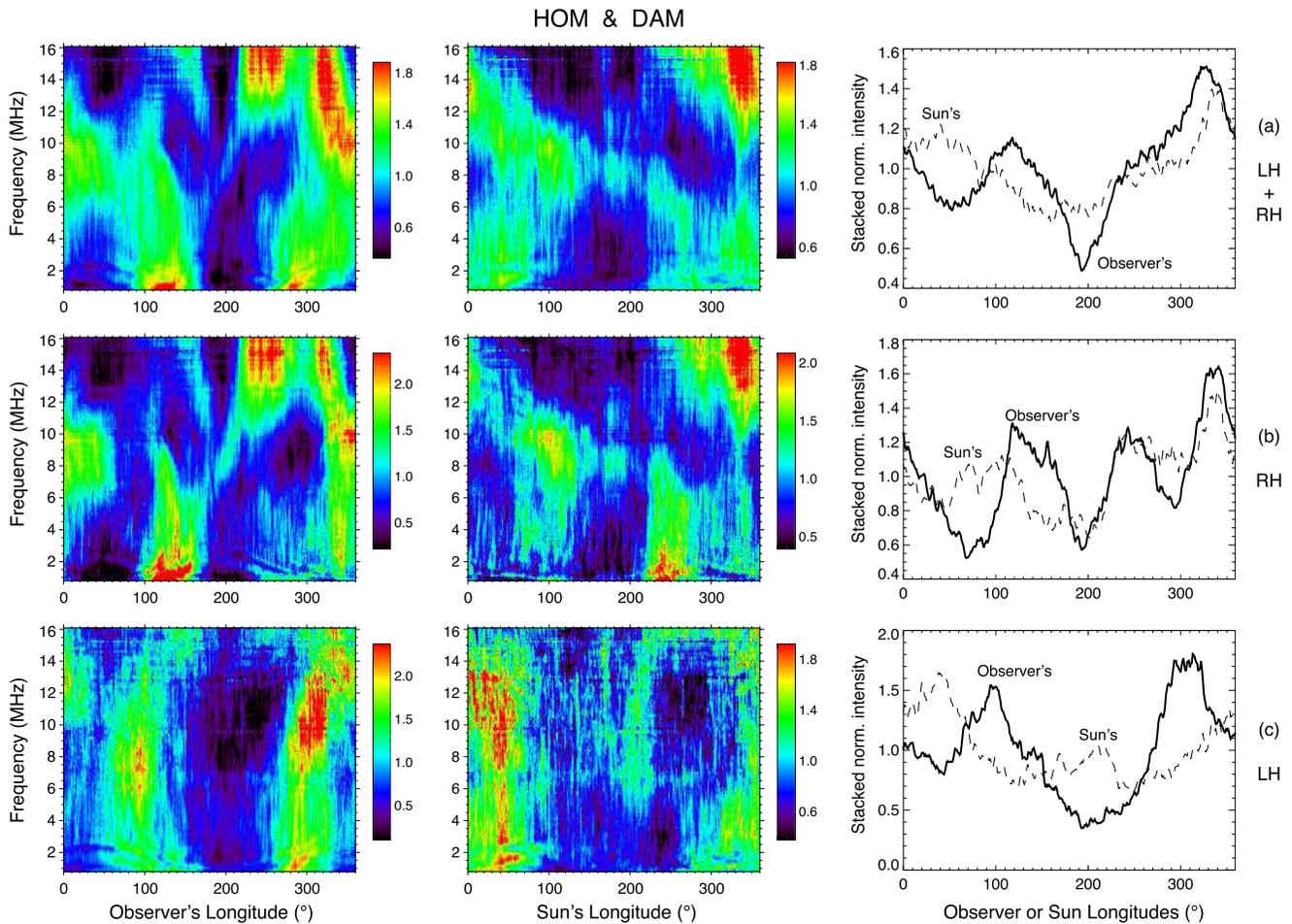
Figure 4. Stacking of RPWS measurements of HOM and DAM emission over the entire Cassini-Jupiter flyby in the range 0.8–16.1 MHz. In the first column, the dynamic spectrum is stacked as a function of Observer's longitude (in 1° wide bins). Each line of the dynamic spectrum has been divided by its average value, equalizing the contrast at all frequencies, as defined in Figure B1b. In the second column, stacking is similarly done, but as a function of the Sun's longitude. On the average, each pixel of these dynamic spectra corresponds to the stacking of ≥430 RPWS measurements. The contrast of the display is slightly stretched relative to Figure 3, for enhancing the various components. In the third column, the two curves in each panel result from the integration over all frequencies of the two dynamic spectra on the same line, and show intensity profiles versus longitude (Observer's = solid line, Sun's = dashed line). These profiles have been smoothed over three consecutive pixels in order to reduce the influence of small spikes. Row (a) corresponds to RH + LH polarized emissions ($0.02 \leq |V| \leq 1.05$), row (b) to RH emissions only ($-1.05 \leq V \leq -0.02$) and row (c) to LH emissions only ($0.02 \leq V \leq 1.05$).

Figure 5 is similar to Figure 4, but for bKOM emissions in the 5–1,000 kHz range (selected from our catalog including only events labeled **bK**). The only differences are: frequencies are in logarithmic scale, the near-CA interval polluted by VLF emissions is excluded, and the intensity scale is in dB above the background (we did not normalized each line of the dynamic spectrum by its average value because this creates large spikes at the upper and lower ends of the dynamic spectra, where little emission is present). For bKOM, it is quite obvious from dynamic spectra and integrated curves that a better contrast is obtained versus Sun's longitude, especially in RH polarization.

In order to quantify the contrast, and thus the "quality of organization" of the data in each longitude system in Figures 4 and 5, we computed 4 contrast indices from each dynamic spectrum. Defining q_N as the $N\%$ quantile, that is, the intensity level exceeded by $N\%$ of the points in a dynamic spectrum, these four indices are: $C_1 = q_5/q_{95}$, $C_2 = q_5 - q_{95}$, $C_3 = q_{10}/q_{90}$ and $C_4 = q_{10} - q_{90}$. We defined two additional indices quantifying the contrast of the integrated profiles in the rightmost column: $C_5 = max/min$ (the ratio between the maximum and minimum values) and $C_6 = max - min$ (their difference). These six indices are computed for each row of Figures 4 and 5. The results are listed in sections "HOM and DAM (all)" and "bKOM (In & Out)" of Table C1.
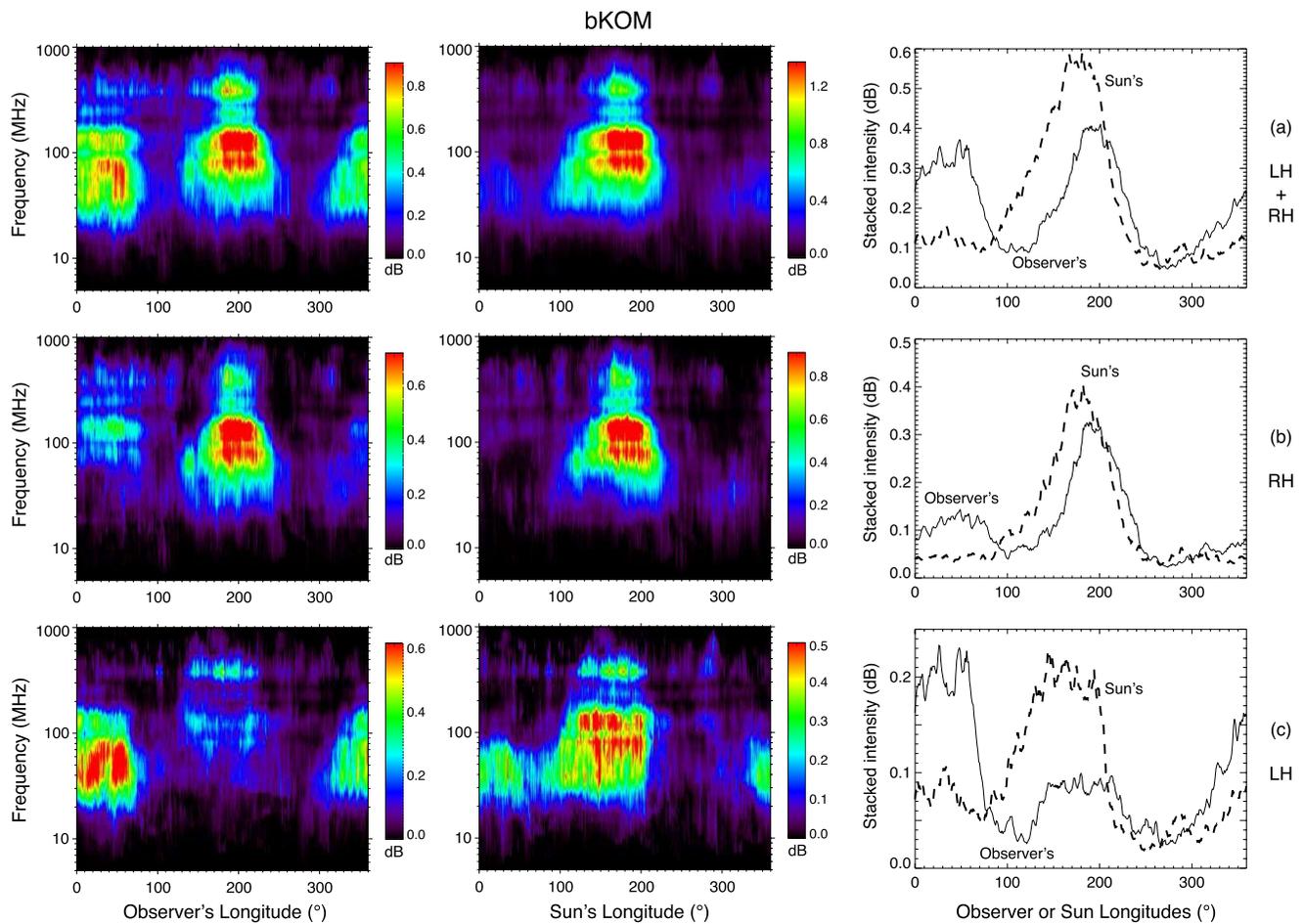
Figure 5. Stacking of RPWS measurements of bKOM emission over the Inbound and Outbound legs of the Cassini-Jupiter flyby in the range 5–1,000 kHz. The format of the figure is identical to that of Figure 4, except for the logarithmic frequency scale and the intensity scale in dB above the background, without equalization of the contrast at the different frequencies (that would create spikes above ~800 kHz and below ~20 kHz).

Figure 6 displays the ratios of contrast indices computed from the data organized in Observer's longitude to those computed from the data organized in Sun's longitude. The better the data is organized by a given longitude system, the higher the value of the corresponding six indices should be. The ratios between the indices computed versus the Observer's longitude and those computed versus the Sun's longitude should thus indicate the relevance of one longitude system with respect to the other.

These ratios are plotted for HOM & DAM in Figure 6a as a separate color line for each data selection of Figure 4 (LH & RH, RH, and LH), for each of the 6 above indices in abscissa. The thick black line is the average of the three color lines. The figure shows that the contrast obtained as a function of Observer's longitude dominates by 10%–20% the contrast obtained as a function of the Sun's longitude. In order to better distinguish the two longitude systems, we re-computed the six indices only for the near-CA interval, during which both systems drift regularly with respect to each other (cf. Figure 1). The results are listed in section "HOM and DAM (CA)" of Table C1, and their ratios are plotted in Figure 6b. Now, the contrast obtained as a function of Observer's longitude dominates by ~50% that obtained as a function of the Sun's longitude. We obtained similar results (not displayed) separately for HOM and DAM, on frequency ranges 0.8–3, 1–7, and 8–16.1 MHz. We also note that the attenuation lane below 4 MHz is better contrasted versus Observer's longitude, which confirms its clear rotational control.

We interpret these results as HOM and DAM sources behaving primarily as rotating searchlights, thus strongly controlled by the rotation of Jupiter. However, as the displayed ratios are not ≫1, a secondary control by the solar wind also exists (Genova et al., 1987; Zarka & Genova, 1983), that we can interpret as
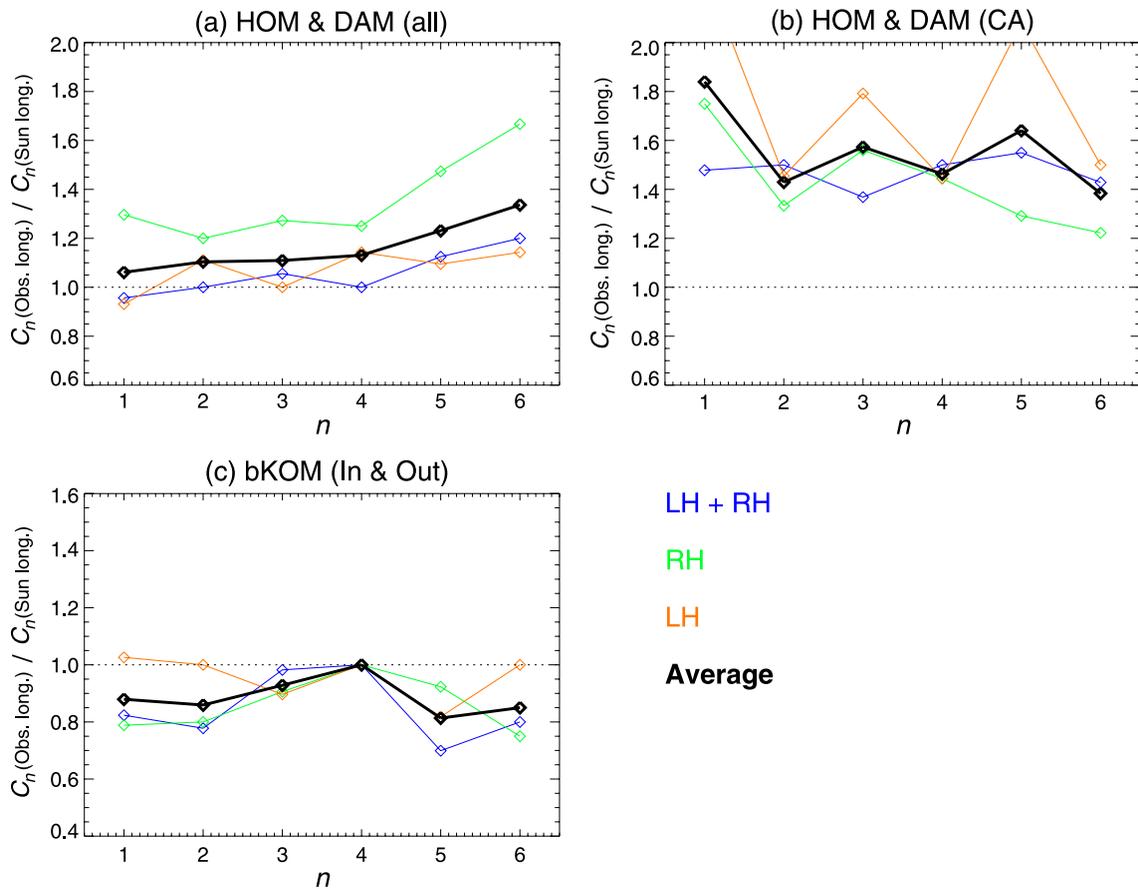
Figure 6. Ratios of the 6 contrast indices C_n (from Table C1) computed from the data organized in Observer's longitude to those computed from the data organized in Sun's longitude, as a function of index number n: (a) from stacked RPWS measurements of HOM and DAM over the entire Cassini-Jupiter flyby in the range 0.8–16.1 MHz (Figure 4); (b) same as (a), but restricted to the near-CA interval (cf. Figure 1); (c) from stacked RPWS measurements of bKOM over the Cassini-Jupiter inbound and outbound legs (excluding the near-CA interval) in the range 5–1,000 kHz (Figure 5). Ratios are plotted with a separate color line for each data selection of Figures 4 and 5 (LH & RH, RH, and LH). Their average is displayed as a thick black line.

the intensity of the emissions being enhanced when their sources sweep across an "active" LT sector of the Jovian magnetosphere. This is somewhat similar to the behavior of Saturn's auroral radio sources described in (Andrews et al., 2011; Lamy, 2011; Lamy et al., 2013). Temporal variations of Io's torus density may also play a role (e.g., Tsuchiya et al., 2019).

Conversely, Figure 6c shows that for bKOM, the indices obtained as a function of Observer's longitude are 10%–20% smaller than those obtained as a function of the Sun's longitude. We conclude that although bKOM is somewhat controlled by the rotation of Jupiter, a dominant—strobe-like—LT effect superimposes, that can be attributed to the solar wind interaction with Jupiter's magnetosphere. This is consistent with the fact that bKOM originates from more external regions of the magnetosphere than HOM and DAM (Ladreiter et al., 1994; Louis, Prangé, et al., 2019; Zarka, 1998).

In both cases, the contrast ratios displayed in Figure 6 are neither ≫1 nor ≪1, thus both internal (rotation) and external (LT or solar wind) control exist for all auroral radio components. In order to further quantify these controls, we propose to represent the rotational modulation of intensity I as:

$$I/I_{max} = 1 - A_i + A_i \left(\frac{1 + cos(\lambda - \lambda_s)}{2} \right)^{\alpha} \tag{1}$$

with λ the Observer's longitude, λ_s the rotating source longitude, A_i the amplitude of the internal control (from 0 = none to 1 = full) and α controlling the searchlight beam width w (we determined that

$\alpha = (190°/w)^2$ implies that the function $\left(\dfrac{1 + cos(\theta)}{2}\right)^{\alpha}$ has a width at half-maximum $\sim w$ degrees). Similarly we propose to represent the solar-wind (LT) control as:

$$I/I_{max} = 1 - A_e + A_e W_{LT}(\lambda_s) \tag{2}$$

with A_e the amplitude of the external control (from 0 = none to 1 = full) and $W_{LT}(\lambda_s)$ a boxcar function = 1 when the source longitude λ_s is within an "active" LT sector $[LT_{min}, LT_{max}]$ and = 0 the rest of the time. In the general case, when both internal and external controls exist, I/I_{max} can be expressed as the product of Equations 1 and 2, that is:

$$I/I_{max} = \left[1 - A_i + A_i\left(\dfrac{1 + cos(\lambda - \lambda_s)}{2}\right)^{\alpha}\right] \times [1 - A_e + A_e W_{LT}(\lambda_s)] \tag{3}$$

We performed a parametric study of this representation of the emission modulation along the parts of Cassini's trajectory corresponding to Figures 6b and 6c. We tested two values of λ_s (100° & 250°), 9 values of w (10°–170° by 20° steps), six values of LT_{min} (0–20 hr by 4 h steps), 12 values of $\Delta LT = LT_{max} - LT_{min}$ (1–12 hr), and 11 values of A_i and of A_e (0–1 by steps of 0.1), totaling 156,800 parameter sets (λ_s, w, LT_{min}, ΔLT, A_i, A_e). For each tested set, we computed the modulation resulting from Equation 3 along the relevant part of Cassini's trajectory, and then stacked it as a function of the Observer's longitude and the Sun's longitude, to obtain stacked intensity curves similar to those in the rightmost column of Figures 4 and 5. From these curves, we computed the corresponding contrast indices C_5 (max/min) and C_6 ($max - min$), and finally their ratio as in Figure 6. We found that the results depend mainly on the amplitudes A_i and A_e, and quite little on parameters λ_s, w, LT_{min} and ΔLT.

Figure 7a displays the distribution of the ratio C_6(Observer's longitude)/C_6(Sun's longitude) for the parametric study along the near-CA trajectory. This ratio covers the range 0–7. Restricting to ratios consistent with the one found in Figure 6b, we found that the distribution of the parameters leading to a ratio 1.5 ± 0.05 is nearly flat for all parameters, except for the amplitudes A_i and A_e, that are furthermore covariant (a broad beam width $w \geq 120°$ is also favored). Figure 7b displays the distribution of amplitudes A_i and A_e corresponding to the study of Figure 7a, that lead to the ratio 1.5 ± 0.05 found in Figure 6b. Equal internal and external controls would lead to peak values along the first diagonal of Figure 7b, pure internal control would lead to peak values at ($A_e = 0$, $A_i > 0$), and pure external control to the symmetrical situation. Here Figure 7b shows that internal (rotational) control of HOM and DAM is largely favored. From the weighted average displayed as the dashed line of slope ~0.3, we estimate that the internal control of HOM and DAM is 3–4 times stronger than external (solar wind) control. The value $A_e = 0$ is not excluded but it is unlikely due to the presence of the gray triangular region above the horizontal black line.

Figure 7c is similar to Figure 7a, but results from a parametric study restricted to the inbound and outbound legs of Cassini's trajectory, excluding the near-CA interval. Figure 7d displays the distribution of amplitudes A_i and A_e corresponding to Figure 7c, that lead to the ratio ~0.85 found in Figure 6c. Here the covariance between A_i and A_e is even more clear, with $A_e \simeq A_i + 0.2$, implying that for bKOM, external (solar wind) control slightly dominates (by a factor that we estimate ~1.3, consistent with the dashed line) over internal (rotational) control. Again the distributions of the other parameters (λ_s, w, LT_{min}, ΔLT) leading to a ratio 0.85 ± 0.05 are nearly flat.

These results demonstrate the different behaviors of HOM + DAM and bKOM emissions, and further emphasize their spectral separation. The model described by Equation 3 is very simplified. It assumes emission in the radial direction from a source at longitude λ_s, which is generally not the case (Zarka, 1998). It can be easily modified to introduce a radio beaming angle relative to the field line carrying the source (Louis, Hess, et al., 2019), or a source extending over a range of longitudes, that could be constrained by UV observations (Louis, Prangé, et al., 2019). But we see that it provides a way to interpret the statistical information conveyed by the stacked plots of Figures 4 and 5.
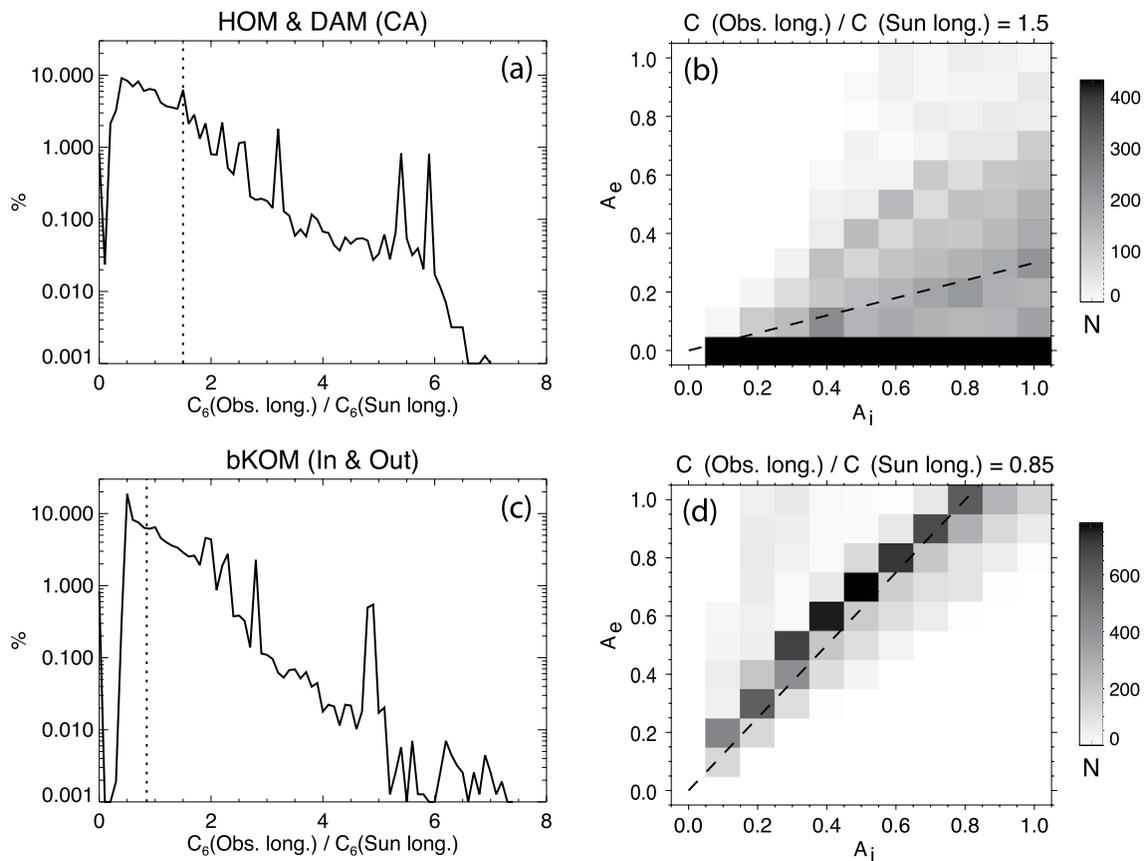
Figure 7. Summary results of the parametric study described in the text for modeling the superimposed internal and external controls of Jovian auroral radio components. (a) Distribution of the computed ratio C_6(Observer's longitude)/C_6(Sun's longitude) along the near-CA trajectory. (b) Distribution of the couples of amplitudes (A_i, A_e) from study (a) and Equation 3 that lead to a ratio 1.50 ± 0.05 (dotted line in (a)). The dashed line is the linear fit (with a constant set to 0) to the weighted average in each column. (c) Same as (a) but computed along inbound and outbound legs of Cassini's trajectory only. (d) Distribution of couples (A_i, A_e) from study (b) that lead to a ratio 0.85 ± 0.05 (dotted line in [c]), and linear fit to the weighted average in each column.

6. Identification of Radio Components and Their Relationships

Let us now identify the components that show up in the dynamic spectra of Figures 3 and 4. Imai et al. (2011) attempted to do so (cf. Figure 3a), but they did not benefit from the polarization information that we derived from RPWS measurements. Thus they simply relied on the Observer's longitude ranges covered by the emissions at the highest RPWS frequencies (~16.1 MHz) and compared it to known ranges corresponding to so-called A, B, C, and D components of auroral DAM (e.g., Carr et al., 1983; Genova et al., 1989).

Besides polarization, we have another important source of information on these DAM components that is the Nançay Decameter Array catalog of Jovian DAM of Marques et al. (2017). The published catalog encompasses 26 years (1990–2015) but it was subsequently extended to 29 years (1990–2018). In this catalog, each emission event is identified and labeled unambiguously (Io or non-Io, and A, B, C, or D...), based on its time-frequency morphology, maximum frequency and polarization. Northern (RH) emissions include Io-induced components A, A', A", B, and B', and auroral (non-Io-) A and B components. Southern (LH) emissions include Io-induced components C and D, and auroral (non-Io-) C and D components. Ganymede-induced emissions were identified by Zarka et al. (2018) and subsequently excluded from auroral ones.

Figure 8 shows stacked occurrence distributions (plotted as dynamic spectra, as a function of the Observer's longitude and the frequency), of each of the four auroral DAM components A, B, C, and D separately, from the (extended) catalog of Marques et al. (2017). This is possible because each emission event is labeled individually in the catalog. As emission observed from Earth corresponds to the same geometry as Cassini's inbound leg, along which we cannot distinguish between Observer's longitude and Sun's longitude as
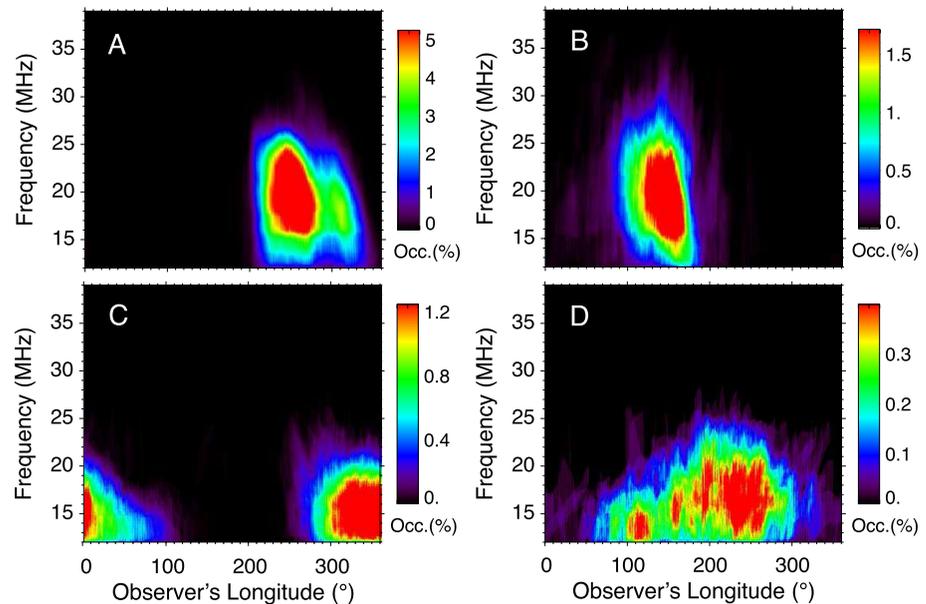
Figure 8. Occurrence probability of each auroral (satellite-independent) DAM component, from the Nançay Decameter Array catalog of Marques et al. (2017), as a function of Observer's longitude (in 1° bins) and frequency (in 100 kHz bins). The number of occurrences of the corresponding emission in each bin is divided by the number of observations performed in the same bin. As seen from Earth, A & B originate from the Northern hemisphere, C & D from the South, B & D from the dawn side, and A & C from the dusk side of the magnetosphere.

explained above for Figure 3, we only plot stacked emission occurrence versus the Observer's longitude that is the most relevant coordinate to compare with Cassini data. Occurrence is used as it provides a very fine measure of emission activity over the 29 years studied. Over 25,000 rotations are stacked in each panel of Figure 8. Component A of auroral DAM (northern hemisphere, post-meridian side, i.e., dusk side as seen from Earth) has the highest occurrence probability, and it is clearly split in 2 sub-components, below and above ~290° longitude, the latter superimposing to the C component from the southern hemisphere. We further discuss them below. Component D is spread in longitude and has low occurrence probability.

Finally in Figure 9, we display composite stacked dynamic spectra of all Jovian auroral components (bKOM, HOM, and DAM) built from Cassini and Nançay data together, in both RH and LH polarizations (central panel), and separately in LH (left panel) or RH (right panel) polarization. Our reprocessed Cassini data from the inbound leg only have been used, because they were recorded in a geometry close to that of Earth-based observations, that is, the displayed Cassini data are a color version of the left panels of Figures B1e, B1f and B1g. Above 16 MHz, occurrence rates from Nançay data are shown, gathering A & B (respectively C & D) panels of Figure 8 in RH (resp. LH) polarization. The higher occurrence of A and B components completely dominates that of C and D components when all are superimposed in the central panel, hence the importance of separating RH and LH polarized emissions. Below 16 MHz detrended RPWS flux densities are stacked versus the Observers's longitude. A linear frequency scale is used from 4 to 16 MHz and a logarithmic scale below 4 MHz, to display clearly all auroral radio components. The intensity scale is in arbitrary units, as it mixes normalized intensities for Cassini and occurrences for Nançay. It has been adjusted to provide a good contrast over the whole panels, with a moderate jump at 16 MHz. The high-frequency patches (above 16 MHz) are identified unambiguously on the basis of Figure 8. They match well lower frequency emissions observed by Cassini below 16 MHz, which allowed us to identify by continuity many features in RPWS dynamic spectra. These features are labeled in Figures 3b–3d (separately for Cassini's inbound and outbound legs).

Comparing Figures 8 and 9 with Figures 3 and 4, we reached the conclusions listed below that are also summarized in Table D1. Note that in Figures 3 and 9, due to the display in relative units of average flux density at each frequency, comparison of LH and RH (or Inbound and Outbound) emissions should not be done relying on the color scales next to the dynamic spectra. Instead, the relative intensity of LH and RH emissions
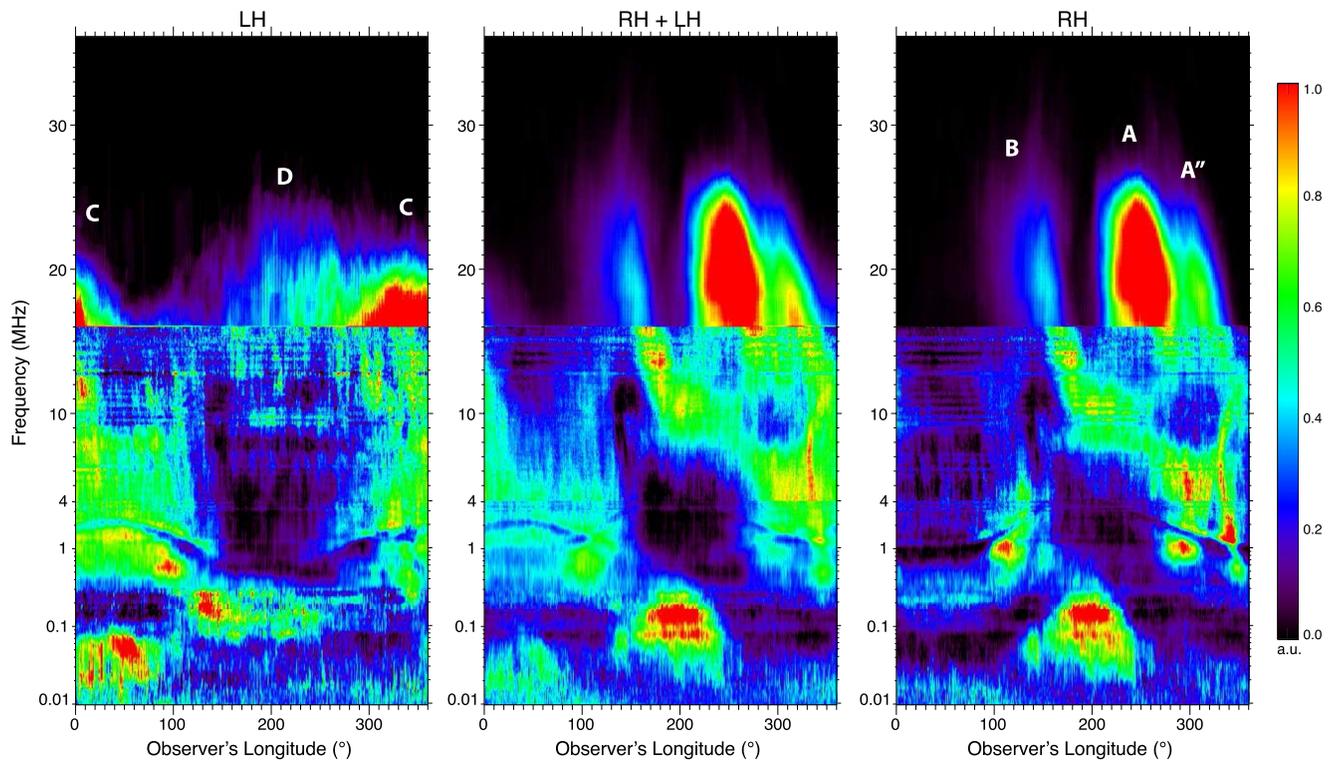
Figure 9. Composite stacked dynamic spectra of all Jovian auroral components (bKOM, HOM and DAM), from inbound Cassini data below 16 MHz and Nançay data above 16 MHz (Marques et al., 2017). A linear frequency scale is used from 4 to 16 MHz and a logarithmic scale below 4 MHz. Longitude bins are 1° wide. Intensity scale is in arbitrary units, mixing normalized intensities for Cassini and occurrence probability for Nançay. It has been adjusted to provide a good contrast over the whole panels. The left panel displays emissions in LH polarization ($0.02 \leq V \leq 1.05$) for RPWS measurements together with C and D emissions from Nançay, whereas the right panel displays emissions in RH polarization ($-1.05 \leq V \leq -0.02$) for RPWS measurements together with A and B emissions from Nançay. The central panel gather bKOM, HOM and DAM, in LH + RH polarization (i.e., it is the sum of the left and right panels).

can be checked by looking at their sum RH + LH on Figures 3 and 9, while the relative intensity of Inbound and Outbound emissions in Figure 3 can be checked by looking at their sum in Figure 4 (left column).

1. The A and B components on Figure 3b, left (Inbound) correspond to the main non-Io-A and non-Io-B components in Figure 3a, left (reproduced from Imai et al., 2011).

2. The sub non-Io-A component in Figure 3a, left is actually LH polarized and corresponds without any doubt to D emission (cf. Figure 3d, left).

3. The component noted non-Io-C in Figure 3a actually consists of the superposition of auroral C emission (Figure 3d) with an intense, well defined RH arc at ~340° longitude that extends up to ~14 MHz (noted "?" in Figure 3c, left). This same RH arc is found at the same longitude in the outbound leg (Figure 3c, right) and is thus clearly rotation-controlled. It is reminiscent of the so-called "lesser arcs" identified in Voyager radio measurements (Alexander et al., 1981; Boischot & Aubier, 1981; Boischot et al., 1981), which have a limited frequency extent and did not yet receive a clear physical interpretation.

4. The A component in Figure 3c, left clearly splits in two sub-components, that are not those labeled in Figure 3a, left. Based on their longitude ranges and on comparison with Nançay data (Figures 8 and 9), we confirm the identification of the main A component below 300°, while the component above 300° coincides with the Io-A" component identified by Marques et al. (2017) in RH polarization and in the same longitude range as C emission. We label here accordingly this sub-component A". This non-Io-A" component seems to be also present outbound, albeit weak (Figure 3c, right). It was incorrectly identified as C by Imai et al. (2011) due to the absence of polarization information. We also note from Figures 3c and 4b, left that the RH arc at ~ 340° longitude (the above-mentioned lesser arc) seems to be connected—although with a curvature change—to the A" emission.

5. Weak nested arcs extending up to ~15 MHz are observed inbound around longitude 100° (Figures 3b–3d, left), which did not stand out of the noise in Figure 3a, left. These arcs, labeled "?", do not seem to

have a counterpart outbound (unless it is superposed to the high frequency end of the HOM emission), so that they may be solar wind-controlled. Their frequency extent is again consistent with "lesser arcs." They might merge with B and/or D emissions above 15 MHz (cf. Figure 9). As they show up in both circular polarizations, they may have elliptical polarization.

6. C and D emissions are clearly identified on the LH inbound panels (Figures 3d and 9, left). C emission is continuously connected to HOM emission, while D is detached from it (or related via arches labeled "?" and via C emission). The component labeled "?" on Figure 3d, left around 100° longitude, discussed above, may also be related to C or D emissions, as suggested by Figure 9, left.

7. Outbound, identification of emissions patches is more uncertain. In RH polarization, the outbound counterparts of inbound emission patches seem easy to identify (albeit with longitude shifts that may be attributed to the different latitude of the observer). But actually this identification depends on the assumption that the source rotates with the planet or is fixed in LT. In the former case, the outbound patches should be labeled in the same order as inbound ones, that is, B around CML ~150° and A around CML ~240°. And indeed when considering the pattern formed inbound by the A and B patches, plus the stronger H patch connected to B by an arch of emission and the weaker isolated H patch, this pattern appears to be reproduced as a mirror image outbound. Thus, identification of A and B patches is uncertain outbound. This is why we labeled them both "A/B." The shape of the arcs could in principle help us distinguishing A and B emissions (see Figure 2 of Marques et al., 2017), but it is not easily identifiable in the narrow 12–16 MHz band in Cassini data. The component that we have labeled A" inbound seems to remain present outbound.

8. The emission patch at 6–10 MHz labeled non-Io-D in Figure 3a, right actually has dominant RH polarization and, provided that we can compare inbound and outbound components, its position is also unlikely to be connected to D emission on Figures 8 and 9. Thus we refute its interpretation by Imai et al. (2011) as D emission, but we have no convincing interpretation for that emission patch thus we labeled it "?" on Figures 3b and 3c, right. In LH polarization outbound (Figure 3d, right) a nearby patch at 8–13 MHz centered at ~60° longitude might be related to D emission.

9. Outbound in LH polarization (Figure 3d, right) it is tempting, by analogy with the inbound dynamic spectrum (Figure 3d, left), to label "C" the high-frequency extensions of HOM emission. But their positions in longitude and their shape in the stacked dynamic spectra of Figure 3d are different inbound and outbound, and we do not have any high-frequency reference (like Nançay) at LT ~21.4 hr. Visual examination of the shape of the arcs detected by Cassini along the two legs of its trajectory around Jupiter revealed that C arcs inbound are dominantly "vertex late" (i.e., post-observer's meridian, as usually seen from the Earth, cf. Figure 2 of Marques et al., 2017), whereas arcs from the two DAM extensions on HOM outbound are dominantly "vertex early" (pre-meridian), consistent with D emission. Thus we labeled these emissions "D."

10. Outbound in Figure 3d, right, the origin of the high frequency patches noted "?," that coincide with A and B emissions in RH polarization, is slightly puzzling. They may result from elliptically polarized A and B emissions, that include a LH circular counterpart. Alternately, they may be related to D emission.

11. Finally, bKOM is completely detached from higher frequency emissions (Figure 9). It consists of a main part above ~40 kHz in antiphase with HOM occurrence, and detached patches below ~80 kHz (especially intense in LH polarization) in phase with HOM occurrence.

As a synthesis of the above conclusions 3, 6, & 9, Figure 3d, left reveals that as seen from Jupiter's dayside, HOM emission in LH polarization is the low-frequency extent of C component of auroral DAM, while from the nightside (Figure 3d, right) HOM is the low-frequency extent of the counterpart of this C component, consistent with D emission. Furthermore Figure 3c, left shows that the most intense HOM emission occurs at the same longitude as A & A" components. These facts suggest that all these emissions originate from the dusk side of the Jovian magnetosphere (Hess et al., 2014). In that part of the magnetosphere, the magnetodisc is thicker (Kivelson & Southwood, 2005) and UV aurora are more active (Clarke et al., 2004; Pallier & Prangé, 2001; Prangé et al., 1998). The nonzero values of the amplitude of the external control A_e can be interpreted as the fact that when rotating sources (that may be related for example to the $d|B|/d\lambda$ gradient at field line footprints) cross the dusk-side magnetosphere, their emission is enhanced. The relation between HOM and A, A", & C auroral DAM is also well visible on Figures 4 and 9.

Along Cassini's inbound leg (Figure 3c, left) a connection is also visible in the longitude-frequency plane between the DAM B component and the most intense HOM emission. This apparent connection across a longitude interval of ~120° might be explained by the combination of the emission beaming (Louis, Hess, et al., 2019) with the complex topology of the magnetic field in Jupiter's northern hemisphere (Connerney et al., 2018). Finally both RH HOM patches are connected to the structures identified above as "lesser arcs."

7. Discussion and Perspectives

We have reprocessed 6 months of Cassini-RPWS data recorded around the Cassini fly by of Jupiter that occurred on December 30th, 2000 (Figure 1), removing a residual dependence on the distance to Jupiter and giving thus equal weights to all data across this 6-month interval (Figure A1). We have computed, from goniopolarimetric inversions developed in Meudon, the circular polarization of all received emissions (Figure A2), and then we have compiled for the first time an exhaustive catalog of Jovian radio emissions (including auroral bKOM, HOM, and DAM) detected over these 6 months (Figure 2).

We have built synthetic dynamic spectra of the polarized intensity of these radio components, stacking the data as a function of the longitude and the frequency (Figures B1 and 3), and we have compared the organization of the data as a function of the spacecraft longitude and as a function of the Sun's longitude (Figures 4 and 5). We have defined contrast indices to quantify this comparison (Figure 6), and found that HOM and DAM are dominantly rotation modulated (i.e., behave rather as rotating searchlight beams from sources fixed in Jovian longitude), whereas bKOM is modulated both by rotation and the solar wind but more strongly by the latter (i.e., it shows a strobe-like behavior from rotating sources whose activity is enhanced within a given Jovian Local Time sector). We have proposed with Equation 3 a simple model of the superposed rotational and LT modulations of a radio component, and performed a parametric study that constrains the values of the amplitudes A_i and A_e of the internal and external controls (Figure 7). The stronger solar wind control on bKOM likely results from the fact that its sources lie on field lines with larger apex (on the average) and at larger distances from the planet.

We have built similar frequency-longitude stacked dynamic spectra of the occurrence of auroral DAM observed from Nançay over 29 years (Figure 8), and used them as guidelines to identify individual auroral radio components in the Cassini-RPWS stacked dynamic spectra of polarized intensity (Figure 3). One of the most significant results is that the most intense HOM emission is detected simultaneously with dusk side auroral DAM components (A, A", and C inbound, D outbound). Intense HOM is also connected to the B component by an arch extending over ~120° of longitude, while there is apparently no direct connection between HOM and the D component of DAM as seen from the dayside.

On Figure 3 and on the family portrait of all Jovian auroral radio components that we have assembled in Figure 9, from kilometer to decameter wavelengths (frequencies from 10 kHz to 40 MHz), DAM, HOM, and bKOM components and their interconnections form very stable patterns over hundreds of Jovian rotations. We interpret this as (a) HOM being indeed the low-frequency extent of auroral DAM; the connection is more clear and straightforward in the southern hemisphere where Jupiter's magnetic field is closer to dipolar and more complex, with branches and voids, in the northern hemisphere where the field is more complex and multipolar; and (b) intense HOM emission primarily originates from Jupiter's dusk side magnetosphere.

The next challenge is to simulate—and thus explain—this pattern with the ExPRES code (Louis, Hess, et al., 2019), choosing adequate sources, possibly relying on simultaneous observations of UV auroral hot spots (Louis, Prangé, et al., 2019), within the frame of the recent Jovian magnetic field models JRM09 (Connerney et al., 2018) or future better models. We also noted that HOM seems to be related to the so-called lesser arcs identified in Voyager radio measurements (Alexander et al., 1981; Boischot & Aubier, 1981; Boischot et al., 1981), which have a limited frequency extent, and whose curvature suggests a dawnside origin. Their origin remains to be fully understood, but here again ExPRES simulations could be of great help (see Figures 8 and 10 of Cecconi et al., 2012).

Finally, bKOM appears on Figure 9 completely detached from higher frequency emissions and consists of a main part above ~40 kHz in antiphase with HOM occurrence, and detached patches below ~80 kHz (especially in the south) in phase with HOM occurrence. The stable morphology revealed in the longitude-frequency

plots of Figures 3 and 9, and the overlap between bKOM, HOM, and DAM source field line ranges, similarly suggests that the gap between bKOM and HOM patches results from a combination of source location, beaming, and magnetic field topology, that can be explored again via ExPRES simulations.

With this work, we tried to reduce the entropy of the complex Jovian radio zoo (e.g., Zarka, 1998). As said above, the next step to confirm our conclusions, fully interpret Figures 3 and 9, and further explore the simple model of Equation 3, relies on ExPRES simulations (Louis, Hess, et al., 2019). The studies conducted in this work were limited by the small number of geometries of observation explored during the Cassini-Jupiter flyby (two long—inbound and outbound—legs, and a single closest approach interval). The situation is different with Juno/WAVES observations (Kurth, Imai, et al., 2017). The Juno mission provides an extensive coverage of all Jovian longitudes, latitudes and LT. This is a major strength that compensates for the poor sensitivity of the Waves receiver and the absence of polarization measurements (Kurth, Hospodarsky, et al., 2017).

Following the same approach as in Section 3, we started to build a catalog of Jovian radio components detected in the Juno/Waves data (Louis et al., 2021), the analysis of which should ultimately extend the results of the present paper.

Finally, the catalog and the detrended data computed in this work (with equal weight over the entire Jupiter fly by) will be used for subsequent studies, including e.g., cross-correlations studies between the Jovian radio components to compare their temporal variations. Our catalog will also be a useful input to train machine learning software presently in development, that intend to recognize automatically radio components (Jovian and other) on dynamic spectra.

Appendix A: Detrending and Polarization of Cassini-RPWS Data

Calibrated, background-subtracted, normalized Cassini-RPWS data are displayed in dB above a threshold of 10^{-24} $Wm^{-2}Hz^{-1}$ in Figure A1a, for a typical channel corresponding to the frequency 120 kHz. The data gaps are set to the arbitrary value -1. Figure A1a reveals a residual trend as a function of the distance to CA, and occasionally lower values due to RPWS mode changes between Monopole (~79% of the time), Dipole (~5%), and Mixed (~5%). Gaps represent ~11% of the time.

In order to improve the quality of our subsequent analysis of these data, we detrended this residual variation in each channel: a daily background was recomputed separately for each of the three above RPWS modes and subtracted, and then isolated spikes $<-4\sigma$ or $>10\sigma$ were interpolated on surrounding values at the same frequency. Detrended data cover quite homogeneously the range 0 to ~50 dB (0–30 dB at 120 kHz, as displayed on Figure A1b), and thus have all the same weight along the entire Cassini trajectory. Note that the 0 dB value is modified by the detrending. Gaps are still left at -1.

An alternate detrending procedure was also tested: it includes equalization of recomputed backgrounds to the one in Monopole mode (but no background subtraction), followed by spikes elimination as above, subtraction of a polynomial (parabolic) fit of the residual long term variation, equalization of intensity histograms at each frequency relative to each other, and a second pass of spikes elimination. This more complex procedure gave results very similar to the previous one, only better preserving very low values down to -20 dB of the Galactic background (that are rather set to 0 dB with the previous procedure). As our subsequent study will be largely dominated by strong emissions, we selected the first, simpler detrending method for the present study.

The Cassini-RPWS-HFR receiver provides auto- and cross-correlation signals between the RPWS electric antennas, that allowed us to retrieve the polarization of the incoming waves, and especially its circular polarization V, in principle comprised in the interval $-1 \le V \le 1$. Figure A2a shows the resulting histograms of values of V over the 6-month interval studied, within 1% bins. About 30% of the data correspond to unpolarized measurements ($|V| < 1\%$), that include absence of emission (background) and Solar type III bursts. The histogram is symmetrical, consistent with the North-South symmetry of Jovian radio emissions and that of Cassini's trajectory, and it steadily decreases toward $V = \pm 1$. Restricting the frequency interval
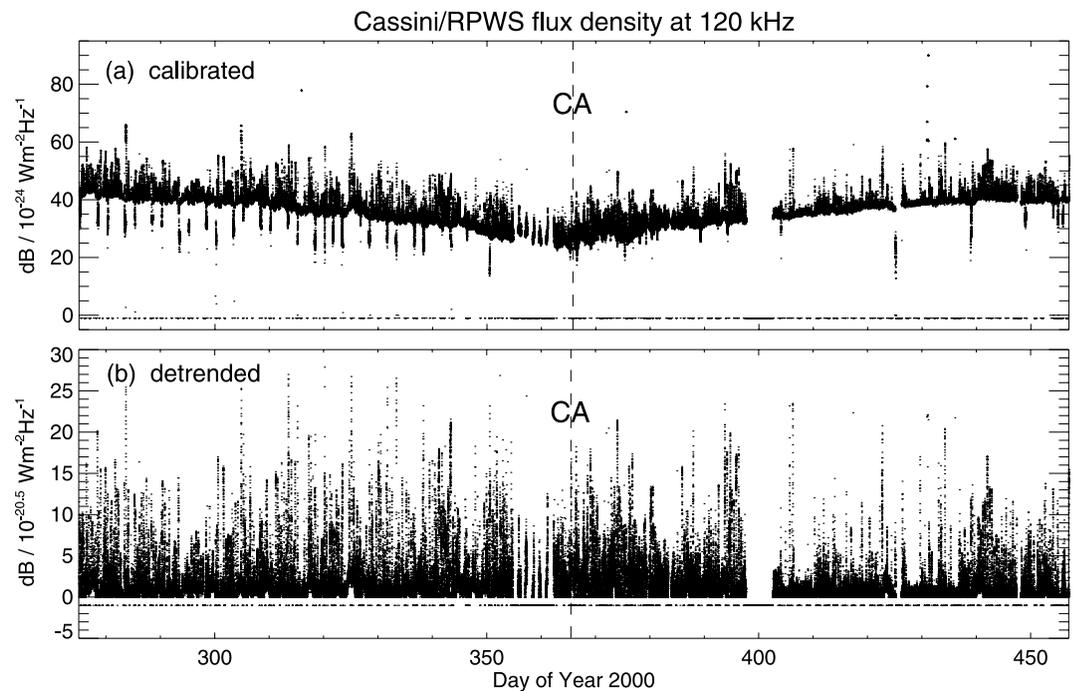
Figure A1. Detrending of RPWS flux density time series. (a) Time series at 120 kHz calibrated as in Zarka et al. (2004), in dB above 10^{-24} $Wm^{-2}Hz^{-1}$. A residual trend subsists as a function of the distance to CA (DoY 365.417), and series of lower values (especially inbound) are due to RPWS mode changes. Gaps are set to −1 and represent ∼ 11% of the time. (b) Detrended time series at 120 kHz (following the first method described in the text), in dB above $10^{-20.5}$ $Wm^{-2}Hz^{-1}$. No residual time variation is left. Gaps are still at −1.

to the range <4 MHz (where values of V are most reliable) produces a similar histogram, the only difference being an excess of positive (LH) values. This suggests that more emissions were detected from the southern hemisphere, but this conclusion must be mitigated by the fact that ∼25% of the inbound observations were recorded in a mode that does not allow to retrieve V, versus only ∼14% outbound.

The histogram of Figure A2a also shows that Jovian radio emissions are elliptically ($|V| < 1$) to fully circularly ($|V| ∼ 1$) polarized. Unphysical values with ($|V| > 1$) represent a small fraction (2.4%) of the total number of measurements. We set arbitrary limits at ±1.5 for the results of the inversion. Dashed lines indicate the limits of the intervals that we considered as the significant ranges for RH ($−1.05 \le V \le −0.02$) and LH ($+0.02 \le V \le +1.05$) polarization. The limit at ±1.05, slightly above the physical limit at ±1, takes into account the numerical uncertainty of the inversions. The limit at ±0.02 is much lower than for example in Lamy et al. (2008) (±0.2), because we do not want here to quantitatively study V but only use it for selecting the largest possible fraction of useful signal, whereas Lamy et al. (2008) restricted their quantitative study to emissions with SNR > 10.

Figure A2b shows histograms of measured flux densities, independent of the polarization (solid line), RH (dashed) and LH (dotted). RH and LH distributions are nearly identical, again revealing the North-South symmetry of Jovian radio emissions.
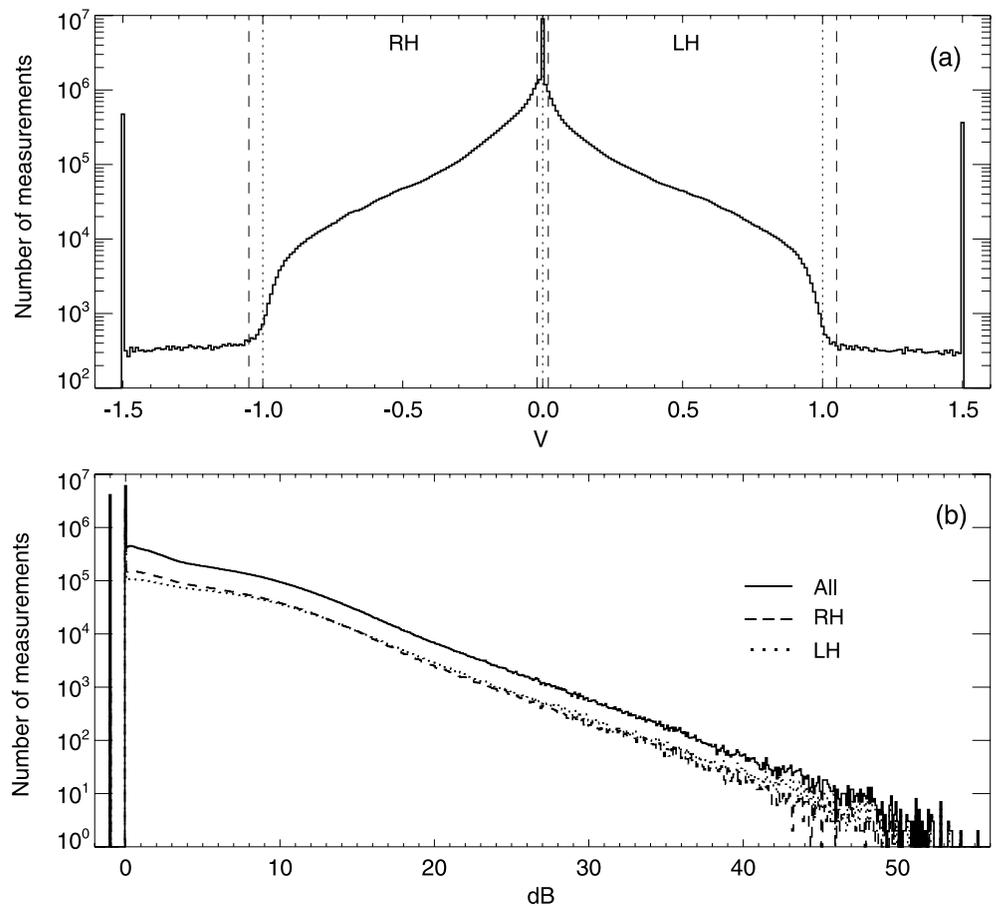
Figure A2. Distributions of circular polarization and calibrated intensities measured by Cassini-RPWS-HFR at Jupiter. (a) Histogram of circular polarization (V) values. The peak at $V = 0$ corresponds to unpolarized measurements (background, Solar type III bursts). Inversion results are arbitrarily limited to ±1.5. Dotted lines indicate V = 0, ±1. Dashed lines delimit our defined ranges of RH ($-1.05 \leq V \leq -0.02$) and LH ($+0.02 \leq V \leq +1.05$) polarized emissions. (b) Histograms of measured flux densities, independent of V (All = solid line), RH polarized (dashed line), and LH polarized (dotted line).

Appendix B: Stacked Intensity Dynamic Spectra

We searched an optimal way to obtain and display stacked intensity plots as a function of longitude and frequency. Our tests are summarized in Figure B1, where all plots are stacked versus Observer's longitude and frequency. The frequencies cover the range 5–16,125 kHz following a logarithmic scale, and longitude bins are 1° wide.

Results are presented in three columns and seven rows. The first column corresponds to the inbound leg of Cassini's trajectory, the second column to the near-CA interval, and the third column to the outbound leg, as defined in Figure 1.

Row (a) is obtained without any selection, just by stacking all data. The gray scale is linear, in multiples of $10^{-20.5}\ Wm^{-2}Hz^{-1}$ at 1 AU from Jupiter. The different contrast below and above 320 kHz, in all three panels of row (a), results from the different channel widths and sensitivities of RPWS on either side of this frequency. Also, nKOM is a weak component and bKOM is very sporadic, so both show up weakly in the plots. Solar type III bursts are prominent inbound, and VLF (Non thermal continuum [Gurnett & Scarf, 1983] and Quasi-Periodic bursts [MacDowall et al., 1993]) are very intense below ~100 kHz near CA. Row (b) corresponds to the same selection as row (a), but each line of the dynamic spectrum has been divided by its average
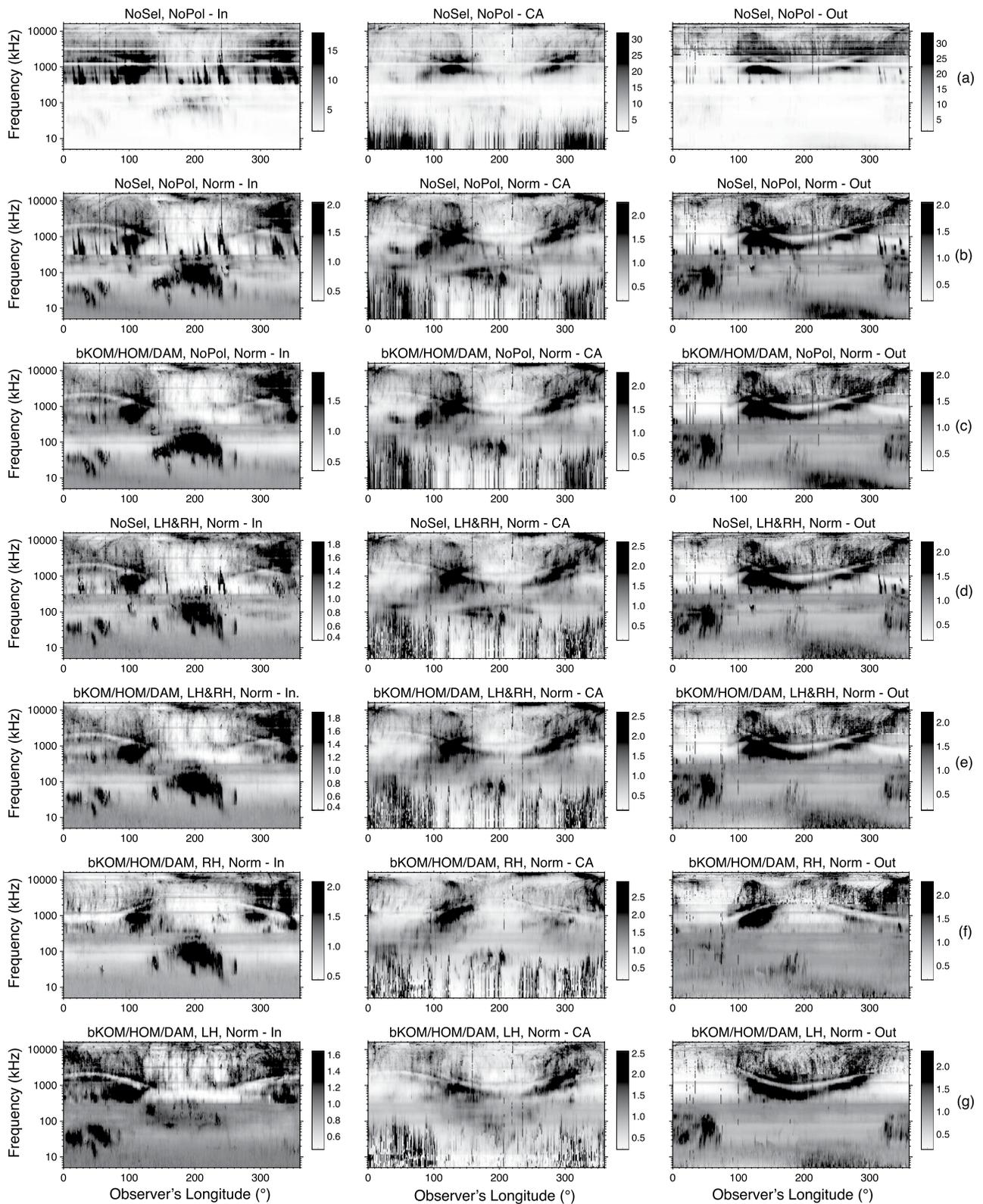
Figure B1.

value, equalizing the contrast at all frequencies. The gray scale, still linear, is now in units of average flux density at each frequency. This same display is used for all subsequent rows.

Row (c) results from a selection of auroral components bKOM, HOM and DAM from our catalog (excluding **nK**, **T3**, **Io**, **Sa**, and **An** events, as explained in Section 3). Type III bursts are almost completely eliminated and the contrast is improved on Jovian auroral components. Emission patches at 100–200 kHz, especially visible near-CA, that correspond to nKOM emission, are also automatically eliminated. Row (d) is obtained from a selection in polarization only, using the intervals $0.02 \leq |V| \leq 1.05$. Type III bursts are again eliminated, but not as well as in row (c), and weak nKOM emission subsist in the range 100–200 kHz, as well as polarized spikes not identified as bKOM, HOM, or DAM. The VLF emissions have their intensity reduced (thus they are partly unpolarized or linearly polarized). Row (e) combines the selections of rows (c and d). We will use this selection that gives the clearest dynamic spectra.

The last two rows, respectively (f) and (g), split the dynamic spectra of row (e) in resp. RH and LH polarized auroral emissions. The auroral Jovian components show up very clearly in all panels of these two rows, except at low frequencies near CA, where they are obscured by the above mentioned VLF sporadic emissions. We will thus exclude the near-CA interval when stacking emission at low frequencies over the entire flyby. Each column of Figure B1 corresponds to about 2 months of stacked Jovian rotations, resulting in 150 ± 30 measurements in each 1° wide bin of all dynamic spectra. The stacked frequency-longitude plots correspond thus to a good statistical description of the data.

The last three rows demonstrate the interest of separating the data as a function of their circular polarization sense (sign of V). The two superimposed attenuation lanes (Gurnett et al., 1998; Menietti et al., 2003) in phase opposition in row (e) split in one lane in each polarization (corresponding to each hemisphere) in rows (f) and (g). The multiple patches of bKOM in the range ~20–400 kHz in row (e) nicely split in one main patch per polarization (thus per hemisphere for X-mode radiation) in rows (f) and (g). VLF emissions (not studied here) also show a different distribution in longitude for RH and LH polarizations.

Arc shapes with both curvatures are visible in the DAM range, that are partly (but not systematically) connected to HOM at their lower end, but the time-frequency structure of HOM looks different from that of DAM. Differences in the distribution of emission patches in the three columns reveal a behavior not consistent with a strict rotational control of the emissions. In the case of such a strict control, emissions would behave like searchlight beams and the dynamic spectra in the three columns should look very similar. While this is the case for RH HOM, it is less true for LH HOM and even less true for bKOM in both polarization senses. Of course, the difference in the spacecraft latitude inbound and outbound may also modify the morphology of the emissions (Barrow, 1981; Desch & Kaiser, 1980).

Figure B1. Overview of stacked frequency-longitude plots for various catalog and/or polarization selections. The frequencies cover the range 5–16,125 kHz following a logarithmic scale, and longitude bins are 1° wide. The 3 columns correspond to inbound [In], near-CA [CA] and outbound [Out] intervals. Row (a) [NoSel, NoPol] was obtained without any selection, just by stacking all data. The gray scale is linear, in multiples of $10^{-20.5} \, Wm^{-2}Hz^{-1}$ at 1 AU from Jupiter. Row (b) [NoSel, NoPol, Norm] corresponds to the same selection as row (a), with each line of the dynamic spectrum divided by its average value, equalizing the contrast at all frequencies. The gray scale, still linear, is now in relative units of average flux density at each frequency. This display is used for all subsequent rows. Row (c) [bKOM/HOM/DAM, NoPol, Norm] results from a selection of auroral components bKOM, HOM and DAM from our catalog. Row (d) [NoSel, LH&RH, Norm] is obtained from a selection in polarization only, using the intervals $0.02 \leq |V| \leq 1.05$. Row (e) [bKOM/HOM/DAM, LH&RH, Norm] combines the selections of rows (c) and (d). Rows (f) [bKOM/HOM/DAM, RH, Norm], and (g) [bKOM/HOM/DAM, LH, Norm] split the dynamic spectra of row (e) in resp. RH and LH polarizations.

Appendix C: Data Organization in Observer's and Sun's Longitude Systems

Table C1 lists the values of the s contrast indices (defined in Section 5) computed from the dynamic spectra and line plots in each row of Figures 4 and 5. The results are listed in sections "HOM and DAM (all)", "HOM and DAM (CA)" and "bKOM (In & Out)".

Table C1
Indices C_1 to C_6 Characterizing the Contrast of HOM and DAM Dynamic Spectra and Line Plots of Figure 4, and of bKOM Dynamic Spectra and Line Plots of Figure 5

	Observer's longitude						Sun's longitude					
	C_1	C_2	C_3	C_4	C_5	C_6	C_1	C_2	C_3	C_4	C_5	C_6
HOM and DAM (all)												
LH & RH	2.2	0.8	1.9	0.6	1.8	0.6	2.3	0.8	1.8	0.6	1.6	0.5
RH	3.5	1.2	2.8	1.0	2.8	1.0	2.7	1.0	2.2	0.8	1.9	0.6
LH	2.7	1.0	2.2	0.8	2.3	0.8	2.9	0.9	2.2	0.7	2.1	0.7
HOM and DAM (CA)												
LH & RH	3.4	1.2	2.6	0.9	3.1	1.0	2.3	0.8	1.9	0.6	2.0	0.7
RH	5.6	1.6	3.9	1.3	3.1	1.1	3.2	1.2	2.5	0.9	2.4	0.9
LH	7.1	1.6	4.3	1.3	5.2	1.5	3.1	1.1	2.4	0.9	2.5	1.0
bKOM (In & Out)												
LH & RH	7.0	0.7	5.6	0.6	8.6	0.4	8.5	0.9	5.7	0.6	12.3	0.5
RH	4.1	0.4	2.9	0.3	14.4	0.3	5.2	0.5	3.2	0.3	15.6	0.4
LH	3.9	0.4	2.6	0.3	9.9	0.2	3.8	0.4	2.9	0.3	12.1	0.2

Note. Indices computation is defined in the text. Results are given in units of the corresponding panels of Figures 4 and 5.

Appendix D: Summary of the Conclusions Drawn From Figures 3, 4, 8 and 9

Table D1
Conclusions 1–11 of Section 6 are Listed in a Synthetic Form Together With the Figures and Panels on Which They are Based

#	Conclusion	Figure, panel
1	Inbound, our A and B components correspond to non-Io-A (main) and non-Io-B from Imai et al. (2011)	3a and 3b, left
2	Sub non-Io-A component from Imai et al. (2011) is actually D (LH)	3a and 3d, left
3	Non-Io-C component from Imai et al. (2011) is actually the superposition of auroral C (LH) emission with an intense RH, rotation-controlled (lesser?) arc	3a; 3c; 3d
4	Our A component splits in a main (A, <300°) and a secondary (A", >300°) components, the latter seemingly connected with the above RH (lesser?) arc	3a, left; 3c; 4b, left; 8; 9
5	Nested arcs (≤15 MHz, labeled "?") show up ~100° in both polarizations (thus possibly elliptical), without an outbound counterpart (thus solar wind-controlled?)	3b–3d, left
6	C component (LH, that may include the above arcs "?" around 100°) is directly connected to HOM, not D	3d, left; 9, left
7	The pattern formed inbound by A, B, and H components seems reproduced as a mirror image in longitude outbound (suggesting partial solar wind control), hence our labeling of A/B patches outbound; A" is present at the same longitude outbound (suggesting rotation control)	3c
8	Inbound non-Io-D component (6–10 MHz) from Imai et al. (2011) has dominant RH polarization and is thus not D emission (we labeled it "?")	3a–3c, right; 8; 9
9	The counterparts of "vertex late" C arcs inbound are "vertex early" emissions, thus labeled D; both are connected to HOM	3d
10	High frequency patches noted "?" outbound may result from elliptically polarized A and B emissions (or be related to D)	3d, right
11	bKOM is detached from HOM, and consists of a main part >40 kHz in antiphase with HOM, and patches <80 kHz in phase with HOM	9

Data Availability Statement

Data products built for and used in this study are available through the MASER (Measurement, Analysis and Simulation of Emissions in the Radio range) service: https://doi.org/10.25935/2f8g-c505 (Zarka et al., 2021).

References

Alexander, J. K., Carr, T. D., Thieman, J. R., Schauble, J. J., & Riddle, A. C. (1981). Synoptic observations of Jupiter's radio emissions: Average statistical properties observed by Voyager. *Journal of Geophysical Research*, *86*(A10), 8529–8545. https://doi.org/10.1029/JA086iA10p08529

Andrews, D. J., Cecconi, B., Cowley, S. W. H., Dougherty, M. K., Lamy, L., Provan, G., & Zarka, P. (2011). Planetary period oscillations in Saturn's magnetosphere: Evidence in magnetic field phase data for rotational modulation of Saturn kilometric radiation emissions. *Journal of Geophysical Research*, *116*(A9), A09206. https://doi.org/10.1029/2011JA016636

Bagenal, F., Adriani, A., Allegrini, F., Bolton, S. J., Bonfond, B., Bunce, E. J., et al. (2017). Magnetospheric Science Objectives of the Juno Mission. *Space Science Reviews*, *213*, 219–287. https://doi.org/10.1007/s11214-014-0036-8

Barrow, C. H. (1981). Latitudinal beaming and local time effects in the decametre-wave radiation from Jupiter observed at the earth and from Voyager. *Astronomy and Astrophysics*, *101*, 142–149.

Boischot, A., & Aubier, M. G. (1981). The Jovian decametric arcs as an interference pattern. *Journal of Geophysical Research*, *86*, 8561–8563. https://doi.org/10.1029/JA086iA10p08561

Boischot, A., Lecacheux, A., Kaiser, M. L., Desch, M. D., Alexander, J. K., & Warwick, J. W. (1981). Radio Jupiter after Voyager: An overview of the planetary radio astronomy observations. *Journal of Geophysical Research*, *86*(A10), 8213–8226. https://doi.org/10.1029/JA086iA10p08213

Burke, B. F., & Franklin, K. L. (1955). Observations of a variable radio source associated with the planet Jupiter. *Journal of Geophysical Research*, *60*(2), 213–217. https://doi.org/10.1029/JZ060i002p00213

Carr, T. D., Desch, M. D., & Alexander, J. K. (1983). Phenomenology of magnetospheric radio emissions. In A. J. Dessler, (Ed.), *Physics of the Jovian magnetosphere* (pp. 226–284). https://doi.org/10.1017/cbo9780511564574.009

Cecconi, B., Hess, S., Hérique, A., Santovito, M. R., Santos-Costa, D., Zarka, P., et al. (2012). Natural radio emission of Jupiter as interferences for radar investigations of the icy satellites of Jupiter. *Planetary and Space Science*, *61*(1), 32–45. https://doi.org/10.1016/j.pss.2011.06.012

Cecconi, B., & Zarka, P. (2005). Direction finding and antenna calibration through analytical inversion of radio measurements performed using a system of two or three electric dipole antennas on a three-axis stabilized spacecraft. *Radio Science*, *40*(3), RS3003. https://doi.org/10.1029/2004RS003070

Clarke, J. T., Grodent, D., Cowley, S. W. H., Bunce, E. J., Zarka, P., Connerney, J. E. P., & Satoh, T. (2004). Jupiter's aurora. In F. Bagenal, T. E. Dowling, & W. B. McKinnon, (Eds.), *Jupiter the planet, satellites and magnetosphere* (Vol. 1, pp. 639–670).

Connerney, J. E. P., Kotsiaros, S., Oliversen, R. J., Espley, J. R., Joergensen, J. L., Joergensen, P. S., et al. (2018). A new model of Jupiter's magnetic field from Juno's first nine orbits. *Geophysical Research Letters*, *45*(6), 2590–2596. https://doi.org/10.1002/2018GL077312

Desch, M. D., & Kaiser, M. L. (1980). The occurrence rate, polarization character, and intensity of broadband Jovian kilometric radiation. *Journal of Geophysical Research*, *85*(A8), 4248–4256. https://doi.org/10.1029/JA085iA08p04248

Dessler, A. J. (1983). Physics of the Jovian magnetosphere. Preface. *Physics of the Jovian magnetosphere* (pp. xiii–xvi). Cambridge University Press. https://doi.org/10.1017/CBO9780511564574.002

Echer, E., Zarka, P., Gonzalez, W. D., Morioka, A., & Denis, L. (2010). Solar wind effects on Jupiter non-Io DAM emissions during Ulysses distant encounter (2003–2004). *Astronomy & Astrophysics*, *519*, A84. https://doi.org/10.1051/0004-6361/200913305

Genova, F., Zarka, P., & Barrow, C. H. (1987). Voyager and Nancay observations of the Jovian radio-emission at different frequencies—Solar wind effect and source extent. *Astronomy and Astrophysics*, *182*(1), 159–162.

Genova, F., Zarka, P., & Lecacheux, A. (1989). Jupiter decametric radiation, *Time-variable Phenomena in the Jovian System* (p. 156–174). NASA Special Publication 494.

Gurnett, D. A., Kurth, W. S., Kirchner, D. L., Hospodarsky, G. B., Averkamp, T. F., Zarka, P., et al. (2004). The Cassini radio and plasma wave investigation. *Space Science Reviews*, *114*(1–4), 395–463. https://doi.org/10.1007/s11214-004-1434-0

Gurnett, D. A., Kurth, W. S., Menietti, J. D., & Persoon, A. M. (1998). An unusual rotationally modulated attenuation band in the Jovian hectometric radio emission spectrum. *Geophysical Research Letters*, *25*(11), 1841–1844. https://doi.org/10.1029/98GL01400

Gurnett, D. A., & Scarf, F. L. (1983). Physics of the Jovian magnetosphere. 8. Plasma waves in the Jovian magnetosphere. In *Physics of the Jovian magnetosphere* (pp. 285–316). Cambridge University Press. https://doi.org/10.1017/cbo9780511564574.010

Hess, S., Cecconi, B., & Zarka, P. (2008). Modeling of Io-Jupiter decameter arcs, emission beaming and energy source. *Geophysical Research Letters*, *35*, L13107. https://doi.org/10.1029/2008GL033656

Hess, S. L. G., Echer, E., & Zarka, P. (2012). Solar wind pressure effects on Jupiter decametric radio emissions independent of Io. *Planetary and Space Science*, *70*, 114–125. https://doi.org/10.1016/j.pss.2012.05.011

Hess, S. L. G., Echer, E., Zarka, P., Lamy, L., & Delamere, P. A. (2014). Multi-instrument study of the Jovian radio emissions triggered by solar wind shocks and inferred magnetospheric subcorotation rates. *Planetary and Space Science*, *99*, 136–148. https://doi.org/10.1016/j.pss.2014.05.015

Imai, M., Greathouse, T. K., Kurth, W. S., Gladstone, G. R., Louis, C. K., Zarka, P., et al. (2019). Probing Jovian broadband kilometric radio sources tied to the ultraviolet main auroral oval with Juno. *Geophysical Research Letters*, *46*(2), 571–579. https://doi.org/10.1029/2018GL081227

Imai, M., Imai, K., Higgins, C. A., & Thieman, J. R. (2011). Comparison between Cassini and Voyager observations of Jupiter's decametric and hectometric radio emissions. *Journal of Geophysical Research*, *116*(A12), A12233. https://doi.org/10.1029/2011JA016456

Kivelson, M. G., & Southwood, D. J. (2005). Dynamical consequences of two modes of centrifugal instability in Jupiter's outer magnetosphere. *Journal of Geophysical Research*, *110*(A12), A12209. https://doi.org/10.1029/2005JA011176

Kurth, W. S., Hospodarsky, G. B., Kirchner, D. L., Mokrzycki, B. T., Averkamp, T. F., Robison, W. T., et al. (2017). The Juno waves investigation. *Space Science Reviews*, *213*(1–4), 347–392. https://doi.org/10.1007/s11214-017-0396-y

Kurth, W. S., Imai, M., Hospodarsky, G. B., Gurnett, D. A., Louarn, P., Valek, P., et al. (2017). A new view of Jupiter's auroral radio spectrum. *Geophysical Research Letters*, *44*(14), 7114–7121. https://doi.org/10.1002/2017GL072889

Ladreiter, H. P., Zarka, P., & Lacacheux, A. (1994). Direction finding study of Jovian hectometric and broadband kilometric radio emissions: Evidence for their auroral origin. *Planetary and Space Science*, *42*(11), 919–931. https://doi.org/10.1016/0032-0633(94)90052-3

Lamy, L. (2011). Variability of southern and northern periodicities of Saturn Kilometric Radiation. In H. O. Rucker, W. S. Kurth, P. Louarn, & G. Fischer, (Eds.), *Planetary, solar and heliospheric radio emissions (Pre VII)* (pp. 39–50). https://doi.org/10.1553/PRE7s39

Lamy, L., Prangé, R., Pryor, W., Gustin, J., Badman, S. V., Melin, H., et al. (2013). Multispectral simultaneous diagnosis of Saturn's aurorae throughout a planetary rotation. *Journal of Geophysical Research: Space Physics*, *118*(8), 4817–4843. https://doi.org/10.1002/jgra.50404

Lamy, L., Zarka, P., Cecconi, B., Prangé, R., Kurth, W. S., & Gurnett, D. A. (2008). Saturn kilometric radiation: Average and statistical properties. *Journal of Geophysical Research*, *113*(A7), A07201. https://doi.org/10.1029/2007JA012900

Leblanc, Y., & Daigne, G. (1985). Broadband Jovian kilometric radiation: New results on polarization and beaming. *Journal of Geophysical Research*, *90*(A12), 12073–12080. https://doi.org/10.1029/JA090iA12p12073

Louarn, P., Allegrini, F., McComas, D. J., Valek, P. W., Kurth, W. S., André, N., et al. (2017). Generation of the Jovian hectometric radiation: First lessons from Juno. *Geophysical Research Letters*, *44*(10), 4439–4446. https://doi.org/10.1002/2017GL072923

Louarn, P., Allegrini, F., McComas, D. J., Valek, P. W., Kurth, W. S., André, N., et al. (2018). Observation of electron conics by juno: Implications for radio generation and acceleration processes. *Geophysical Research Letters*, *45*(18), 9408–9416. https://doi.org/10.1029/2018GL078973

Louis, C. K., Hess, S. L. G., Cecconi, B., Zarka, P., Lamy, L., Aicardi, S., & Loh, A. (2019). ExPRES: An exoplanetary and planetary radio emissions simulator. *Astronomy and Astrophysics*, *627*, A30. https://doi.org/10.1051/0004-6361/201935161

Louis, C. K., Lamy, L., Zarka, P., Cecconi, B., & Hess, S. L. G. (2017). Detection of Jupiter decametric emissions controlled by Europa and Ganymede with Voyager/PRA and Cassini/RPWS. *Journal of Geophysical Research*, *122*, 9228–9247. https://doi.org/10.1002/2016JA023779

Louis, C. K., Lamy, L., Zarka, P., Cecconi, B., Hess, S. L. G., & Bonnin, X. (2017). Simulating Jupiter-satellite decametric emissions with ExPRES: A parametric study. In G. Fischer, G. Mann, M. Panchenko, & P. Zarka, (Eds.), *Planetary radio emissions VIII* (pp. 59–72). https://doi.org/10.1553/PRE8s59

Louis, C. K., Lamy, L., Zarka, P., Cecconi, B., Imai, M., Kurth, W. S., et al. (2017). Io-Jupiter decametric arcs observed by Juno/Waves compared to ExPRES simulations. *Geophysical Research Letters*, *44*, 9225–9232. https://doi.org/10.1002/2017GL073036

Louis, C. K., Prangé, R., Lamy, L., Zarka, P., Imai, M., Kurth, W. S., & Connerney, J. E. P. (2019). Jovian auroral radio sources detected in situ by Juno/waves: Comparisons with model auroral ovals and simultaneous HST FUV images. *Geophysical Research Letters*, *46*(21), 11606–11614. https://doi.org/10.1029/2019GL084799

Louis, C. K., Zarka, P., Dabidin, K., Lampson, P.-A., Magalhães, F. P., Boudouma A., et al. (2021). Latitudinal beaming of Jupiter's radio emissions from Juno/Waves flux density measurements. *Journal of Geophysical Research: Space Physics*, *126*, (10). http://doi.org/10.1029/2021ja029435

MacDowall, R. J., Kaiser, M. L., Desch, M. D., Farrell, W. M., Hess, R. A., & Stone, R. G. (1993). Quasiperiodic Jovian Radio bursts: Observations from the ulysses radio and plasma wave experiment. *Planetary and Space Science*, *41*(11–12), 1059–1072. https://doi.org/10.1016/0032-0633(93)90109-F

Marques, M. S., Zarka, P., Echer, E., Ryabov, V. B., Alves, M. V., Denis, L., & Coffre, A. (2017). Statistical analysis of 26 yr of observations of decametric radio emissions from Jupiter. *Astronomy & Astrophysics*, *604*, A17. https://doi.org/10.1051/0004-6361/201630025

Menietti, J. D., Gurnett, D. A., Hospodarsky, G. B., Higgins, C. A., Kurth, W. S., & Zarka, P. (2003). Modeling radio emission attenuation lanes observed by the Galileo and Cassini spacecraft. *Planetary and Space Science*, *51*(9–10), 533–540. https://doi.org/10.1016/S0032-0633(03)00078-3

Pallier, L., & Prangé, R. (2001). More about the structure of the high latitude Jovian aurorae. *Planetary and Space Science*, *49*(10–11), 1159–1173. https://doi.org/10.1016/S0032-0633(01)00023-X

Prangé, R., Rego, D., Pallier, L., Connerney, J., Zarka, P., & Queinnec, J. (1998). Detailed study of FUV Jovian auroral features with the post-COSTAR HST faint object camera. *Journal of Geophysical Research*, *103*(E9), 20195–20215. https://doi.org/10.1029/98JE01128

Reiner, M. J., Fainberg, J., & Stone, R. G. (1993). Source characteristics of Jovian hectometric radio emissions. *Journal of Geophysical Research*, *98*(E10), 18767–18778. https://doi.org/10.1029/93JE01779

Reiner, M. J., Kaiser, M. L., & Desch, M. D. (2000). Long-term behavior of Jovian bKOM and nKOM radio emissions observed during the Ulysses-Jupiter encounter. *Geophysical Research Letters*, *27*(3), 297–300. https://doi.org/10.1029/1999GL003710

Treumann, R. A. (2006). The electron-cyclotron maser for astrophysical application. *Astronomy and Astrophysics Review*, *13*(4), 229–315. https://doi.org/10.1007/s00159-006-0001-y

Tsuchiya, F., Arakawa, R., Misawa, H., Kagitani, M., Koga, R., Suzuki, F., et al. (2019). Azimuthal variation in the Io plasma torus observed by the Hisaki satellite from 2013 to 2016. *Journal of Geophysical Research: Space Physics*, *124*(5), 3236–3254. https://doi.org/10.1029/2018JA026038

Zarka, P. (1998). Auroral radio emissions at the outer planets: Observations and theories. *Journal of Geophysical Research*, *103*(E9), 20159–20194. https://doi.org/10.1029/98JE01323

Zarka, P., Cecconi, B., & Kurth, W. S. (2004). Jupiter's low-frequency radio spectrum from Cassini/Radio and Plasma Wave Science (RPWS) absolute flux density measurements. *Journal of Geophysical Research*, *109*(A9), A09S15. https://doi.org/10.1029/2003JA010260

Zarka, P., Cecconi, B., Magalhães, F. P., Louis, C. K., & Lamy, L. (2021). *Cassini RPWS Jupiter encounter calibrated dataset*. PADC. https://doi.org/10.25935/2f8g-c505

Zarka, P., & Genova, F. (1983). Low-frequency Jovian emission and solar wind magnetic sector structure. *Nature*, *306*(5945), 767–768. https://doi.org/10.1038/306767a0

Zarka, P., Marques, M. S., Louis, C., Ryabov, V. B., Lamy, L., Echer, E., & Cecconi, B. (2017). Radio emission from satellite-Jupiter interactions (especially Ganymede). In G. Fischer, G. Mann, M. Panchenko, & P. Zarka, (Eds.), *Planetary radio emissions VIII* (pp. 45–58). https://doi.org/10.1553/PRE8s45

Zarka, P., Marques, M. S., Louis, C., Ryabov, V. B., Lamy, L., Echer, E., & Cecconi, B. (2018). Jupiter radio emission induced by Ganymede and consequences for the radio detection of exoplanets. *Astronomy and Astrophysics*, *618*, A84. https://doi.org/10.1051/0004-6361/201833586

Zarka, P., Queinnec, J., & Crary, F. J. (2001). Low-frequency limit of Jovian radio emissions and implications on source locations and Io plasma wake. *Planetary and Space Science*, *49*(10–11), 1137–1149. https://doi.org/10.1016/S0032-0633(01)00021-6